

# Design of a Rotary Reactor for Chemical-looping Combustion. Part 2: Comparison of Copper-, Nickel-, and Iron-based Oxygen Carriers.

*Zhenlong Zhao, Ahmed F. Ghoniem\**

Department of Mechanical Engineering, Massachusetts Institute of Technology

77 Massachusetts Avenue, Cambridge, MA 02139-4307, USA

## **Abstract**

Chemical-looping combustion (CLC) is a novel and promising option for several applications including carbon capture (CC), fuel reforming, H<sub>2</sub> generation, etc. Previous studies demonstrated the feasibility of performing CLC in a novel rotary design with micro-channel structures. Part 1 of this series studied the fundamentals of the reactor design and proposed a comprehensive design procedure, enabling a systematic methodology of designing and evaluating the rotary CLC reactor with different OCs and operating conditions. This paper presents the application of the methodology to the designs with three commonly used OCs, i.e., copper, nickel, and iron. The physical properties and the reactivities of the three OCs are compared at operating conditions suitable for the rotary CLC. Nickel has the highest reduction rate, but relatively slow oxidation reactivity while the iron reduction rate is most sensitive to the fuel concentration. The design parameters and the operating conditions for the three OCs are selected, following the

---

\* Corresponding author. Tel.: +1 617 253 2295.

E-mail address: [ghoniem@mit.edu](mailto:ghoniem@mit.edu) (A.F. Ghoniem)

strategies proposed in Part 1, and the performances are evaluated using a one-dimensional plug-flow model developed previously. The simulations show that for all OCs, complete fuel conversion and high carbon separation efficiency can be achieved at periodic stationary state with reasonable operational stabilities. The nickel-based design includes the smallest dimensions because of its fast reduction rate. The operation of nickel case is mainly limited to the slow oxidation rate, and hence a relatively large share of air sector is used. The iron-based design has the largest size, due to its slow reduction reactivity near the exit or in the fuel purge sector where the fuel concentration is low. The gas flow temperature increases monotonically for all the cases, and is mainly determined by the solid temperature. In the periodic state, the local temperature variation is within 40K and the thermal distortion is limited. The design of the rotary CLC is also scaled to different pressures and inlet temperatures. The method of scaling is discussed and desirable operational performances are obtained.

## Keywords

Chemical-looping combustion, rotary reactor, CO<sub>2</sub> capture, oxygen carriers

## Content

Abstract .....	1
Keywords .....	2
Content .....	2
Nomenclature .....	3
1. Introduction .....	5
2. Reactor Design .....	7
3. Model Formulation .....	17

4. Results .....	18
5. Discussion.....	27
6. Conclusion.....	30
Acknowledgement .....	32
Reference .....	33
Appendix A.....	61

## Nomenclature

### Symbols

$A$	cross-sectional area, $\text{m}^2$
$a$	pressure coefficient
$C_i$	concentration of species $i$ , $\text{mol m}^{-3}$
$D$	reactor diameter, m
$d$	channel width, m
$E_a$	activation energy, $\text{J mol}^{-1}$
$E_g, E_s$	energy of gas or solid, $\text{J m}^{-3}$
$H$	channel height, m
$H_g$	enthalpy of gas, $\text{J m}^{-3}$
$h_{gs}$	heat transfer coefficient between phases, $\text{W m}^{-2} \text{K}^{-1}$
$h_{m,i}$	external mass transfer coefficient, $\text{m s}^{-1}$

$\hat{h}_{s,i}$	molar enthalpy for species, J mol <sup>-1</sup>
$k, k_p$	reaction rate constant, m <sup>(3n-3)</sup> mol <sup>(1-n)</sup> s <sup>-1</sup> , n is the reaction order
$k_s, k_g$	thermal conductivity of solid or gas phase, W m <sup>-1</sup> K <sup>-1</sup>
$k_0$	pre-exponential factor, m <sup>(3n-3)</sup> mol <sup>(1-n)</sup> s <sup>-1</sup> , n is the reaction order
$m_{ox}$	mass of fully oxidized oxygen carrier, kg
$m_{red}$	mass of fully reduced oxygen carrier, kg
$n$	reaction order
$P$	operating pressure, Pa
$P_c$	inner perimeter of the channel, m
$p_{i,out}$	partial pressure of species $i$ , Pa
$Q_{gs}$	heat flux from gas phase to solid phase, W m <sup>-2</sup>
$T$	temperature, K
$u$	velocity, m s <sup>-1</sup>
$X$	conversion of oxygen carrier
$x_i$	molar fraction of species $i$

#### Greek letters

$\delta_{bulk}$	thickness of the bulk support layer, m
$\delta_{oc}$	thickness of the porous oxygen carrier layer, m
$\delta_s$	thickness of the solid phase (including the porous layer and the bulk layer), m
$\varepsilon_i$	volume fraction of phase (or species) $i$

$\varepsilon_M$	cross-section area ratio of solid
$\varepsilon_g$	porosity of the solid
$\nu$	stoichiometric coefficient
$\theta_i$	size of sector $i$ , rad
$\rho$	density, kg m <sup>-3</sup>
$\hat{\rho}$	molar density, mol m <sup>-3</sup>
$\tau$	cyclic period time, s
$\omega$	overall molar reaction rate, mol m <sup>-2</sup> s <sup>-1</sup>

#### Acronyms

CC	carbon capture
CLC	chemical-looping combustion
OC	oxygen carrier
Redox	reduction and oxidation

## 1. Introduction

Chemical-looping combustion (CLC) is a novel and promising technology for carbon capture (CC). In CLC, the combustion process is performed in two reactors: a fuel reactor and an air reactor. A solid oxygen carrier (OC) is circulated between these two reactors to transport undiluted oxygen from air to fuel. The exhaust gas from the reduction contains only CO<sub>2</sub> and steam, and pure CO<sub>2</sub> can be readily obtained after water condensation. Using OCs as the looping

medium, the direct contact between air and fuel is circumvented and hence energy-intensive gas separation processes are avoided.

CLC is mostly carried out in two interconnected fluidized-bed reactors with the OC in the form of particles circulating in between [1-7]. Alternatively, a rotary reactor consisting of a large number of micro-channels was proposed in previous studies [8-12]. As shown in Figure 1a, the rotary reactor has a rotary wheel, which rotates through four sectors, i.e., fuel, air, and two steam purging sectors. The wheel consists of a large number of channels (Figure 1b) with the OC coated onto their inner walls. As shown in Figure 1c, the channel wall has two solid layers: a highly porous OC layer and a bulk dense inert substrate. The porous layer consists of active metal oxides, as well as inert binders to maintain the pore structures. Pressurized streams flow through the reactor and react with the OCs to generate the product stream, in this case  $\text{CO}_2/\text{H}_2\text{O}$ , and the oxygen-depleted air stream. A complete description of the reactor design and functionality can be found in refs. [12, 13].

Few studies have been carried out to examine the performances of the rotary reactor for CLC under different conditions [8, 9, 11, 14]. Pavone and co-workers [8, 9] simulated the initial reduction and oxidation (redox) cycles of the reactor with  $\text{NiO}/\text{Al}_2\text{O}_3$  as the OC, and observed 90% separation efficiency but large temperature variations. Zhao et al. [11] examined a copper-based design with a dense boron-nitride support layer, and obtained a stable and periodically stationary performance with complete fuel conversion and carbon separation. However, the behavior strongly depends on the choice of the OCs, the designs, and the operating conditions [14]. From these studies, it is clear that the design of a rotary CLC reactor is a complex process:

many parameters are closely involved and coupled, all of which strongly affect the functionalities of the reactor. Thus, a comprehensive parametric study is important to understand the intrinsic logics and develop the optimized procedures of design under different conditions.

The objective of this two-part series is to investigate the fundamental relations among the design parameters, develop a systematic design procedure, and compare the performances of the design under different conditions. In Part 1, the fundamental effects of the OC characteristics, the reactor configurations, and the operating conditions are examined. A systematic procedure is proposed on the basis of the parametric study. Part 2 presents the application of this procedure to three commonly used OCs, i.e., copper, nickel, and iron. The reaction mechanisms utilized in this study are based on the one-step overall kinetics proposed by Abad and co-workers [15-17]. The redox reactivities of the OCs are analyzed and compared, and their effects on the choice of design are discussed. The performances of rotary reactor with the three OCs are illustrated and the key parameters for each case are identified. The effects of the operating temperature and pressure on the design are also studied and the scaling strategies to different conditions are proposed.

## **2. Reactor Design**

A number of criteria should be satisfied for the design of a rotary reactor, including complete (>99%) fuel conversion, sufficient (>95%) CO<sub>2</sub> separation, and adequate operational stabilities. To achieve these objectives, three groups of parameters can be specified, (i.e., the material selection, the reactor configuration, and the operational conditions), following the procedure

proposed in Part 1 (see Figure 7 in ref. [13]). For the scope of this study, the design focuses on the methane-fueled CLC with a target thermal power output of  $1\text{MW}_{\text{th}}$ .

### ***Operation Specifications***

As pointed out in Part 1, higher operating temperatures are always preferred to obtain better performances and higher system efficiencies. For CLC process, however, concerns over the temperature distribution and fluctuation inside the reactor, which may cause thermal and mechanical stresses at high temperatures, must be addressed. A reasonable operating temperature for CLC is in the range of 1000-1200°C [1, 18]. For the purpose of comparison, the exhaust temperature of the reactor is specified to be around 1200°C and the inlet temperature is 550°C. For the copper-based design, the exit temperature is further constrained below the melting point of copper. The operating pressure of 10 atm is selected on the basis of the system integration [19] with a pilot-level reactor. In Section 5, the designs and performances with different inlet temperatures and operating pressures are also presented.

### ***OC Design***

The active metal oxides used in this study are nickel-, copper-, and iron-oxides, which have been widely suggested as the most promising OC candidates for CLC (e.g., nickel [20-23], copper [16, 20, 23, 24], and iron [20, 25, 26]). Important physical and chemical properties of these metal oxides are summarized in Table 1. The experimental studies performed by Abad and co-workers [15-17] cover a wide range of temperature and pressures for all three OCs using a similar experimental setup. The redox reactivities were analyzed by thermogravimetry (TG) at atmospheric pressure [15, 17] as well as elevated pressures up to 30 atm [16] with the operating



temperature ranging from 773 to 1073 K for the copper-based OC and from 873 to 1223 K for the nickel-, and iron-based OCs. The OCs obtained with the same preparation methods, and thus the same physical (loading content, porosity, tortuosity, active surface area, metal dispersion, grain thickness, inert binder, etc.) and chemical characteristics (chemical kinetics), are used in this study as the OC layers on the channel walls. As seen in Table 1, the copper-based OC prepared by wet-impregnation possesses higher specific surface area and porosity, while the nickel- and iron-based OCs prepared by freeze-granulation have higher loading of active metal oxides.

The reaction mechanism [15-17] is based on the kinetics-controlled unreacted shrinking-core model (USCM), which assumes that within each grain of metal oxide (or metal), as the reaction progresses it leaves behind a layer of product (e.g, Cu for reduction and CuO for oxidation). For the OCs investigated in refs. [15-17], the mass diffusion is fast compared to the chemical reactions such that the active metal oxide (or metal) on the unreacted core surface is exposed to the reactant in the bulk flow. Thus, the redox rates can be expressed as [11, 15, 17, 27],

$$\frac{dX}{dt} = \left( \frac{P}{P_0} \right)^{-a} \frac{\nu_{oc}}{\hat{\rho}_{m,i}} k_0 e^{-E/RT} C_{g,s}^n (X_0 - X)^\beta \quad (1)$$

where  $\hat{\rho}_{m,i}$  is the molar density of the active metal oxide (or metal) grain.  $\nu_{oc}$  is the stoichiometric coefficient.  $k_0$  is the Arrhenius constant.  $C_{g,s}$  is the concentration of the gaseous reactant at the exterior surface of the OC layer and  $n$  is reaction order.  $X$  is the non-dimensional conversion of the OC: it equals zero when the OC is fully reduced and unity when fully oxidized. The term  $(X_0 - X)$  describes the effect of the OC conversion on the redox rates, where  $X_0$  is the final state of the OC conversion ( $X_0$  equals unity for oxidation, and zero for reduction). The geometry

coefficient,  $\beta$ , accounts for structural differences of the active metal oxide grains in the OCs. The active metal oxide in the Fe- and Ni-based OCs prepared by freeze-granulation exhibits a granular grain structure, and the USCM for spherical grains was considered ( $\beta = 2/3$ ), while the USCM for plate-like geometry in the porous surface of the OC was considered for the Cu-based OC prepared by impregnation ( $\beta = 0$ ) [15]. The reaction rate may increase at higher pressure because of the reactant concentration,  $C_{g,s}$  [28-30]. On the other hand, this increase in the reaction rate is lower than expected due to the saturation of gas molecules in the active sites on the grain, as reported in refs. [13, 16]. This pressure-inhibition effect of the operating pressure is described empirically [16] by the term  $(P/P_0)^{-a}$  where  $a$  is the pressure coefficient and  $P_0$  is atmospheric pressure. The overall effect of pressure depends on the contributions from both factors, as showed in Section 5. In Eq.(1), complete fuel conversion is assumed under thermodynamic equilibrium [1, 15, 31] and the reverse reaction and the decomposition of  $H_2O$  (or  $CO_2$ ) into  $H_2$  (or  $CO$ ) are neglected.

The kinetic parameters are listed in Table 1. As an example, Figure 2 shows the typical OC conversion ( $X$ ) profiles as a function of time for the redox reactions of the three OCs. The reduction rate of copper oxide is faster than the other two OCs, while the oxidation rate of copper or iron is faster than that of nickel. The conversion rates of copper are linear with time because of the plat-like grain geometry. In contrast, the reaction rates of nickel and iron depend on the amount of oxygen available in the OC, and as the conversion approaches full reduction or oxidation, the rates decrease significantly. Among these OCs, nickel has the lowest oxidation rate, especially when  $X$  is close to unity. The time required to oxidize nickel from  $X = 0.9$  to  $X = 1.0$  is almost the same with that from 0 to 0.9. Thus, in the design with nickel as OC, an

intermediate range of the OC conversions is used to maintain reasonable reaction rates. From Figure 2, the reduction rate is in general slower than the oxidation rate for the three OCs.

In order to apply the reaction kinetics expressed by Eq.(1), the chemical kinetics must be the rate-limiting step and the mass diffusion within the porous layer should be of limited significance, as in refs. [15-17]. The thickness of the OC layer,  $\delta_{oc}$ , is thus selected to be 50  $\mu\text{m}$ , and the Damköhler number, i.e.,  $Da_{in} = \tau_{in} / \tau_r$ <sup>1</sup>, remains smaller than 0.05 for all the three OCs over a wide range of operating conditions. Therefore, the gas reaction rates can be expressed as:

$$\frac{\omega_{g,i}}{\nu_{g,i}} = \frac{\omega_{oc}}{\nu_{oc}} = \frac{\delta_{oc} \varepsilon_{oc} \hat{\rho}_{m,i}}{\nu_{oc}} \frac{dX_{oc}}{dt} \quad (2)$$

where  $\nu_{g,i}$  is the stoichiometric coefficient for the gas species,  $\varepsilon_{oc}$  is the volume fraction of the active metal in the porous OC layer, and  $\delta_{oc}$  is the thickness of porous OC layer (50  $\mu\text{m}$ ).

As an example, Figure 3 shows the typical gas reaction rate profiles as a function of gas concentration ( $\text{CH}_4$  or  $\text{O}_2$ ) for the redox reactions of the three OCs. Among them, the nickel-based OC has the highest fuel consumption rate. Because of the low active metal oxide loading ( $x_{MeO}$ ), copper has an intermediate reduction rate although the conversion rate of OC is fastest (Figure 2). Within the majority of the fuel concentration range, the fuel consumption rate of iron is the lowest. The reduction rates of nickel and iron strongly depend on the local fuel concentration, and therefore in the CLC process, a higher feed concentration at the inlet is preferred. In contrast, the copper reduction rate is less sensitive to the fuel concentration. All the OCs have a higher oxygen consumption rate as compared to the fuel consumption rate, also seen

---

<sup>1</sup>  $\tau_{in}$  is the characteristic time of conversion in an internal-diffusion controlled process, and  $\tau_{in}$  is the that in kinetics-controlled conversion, as calculated in Eq. (1). See Part 1 for details.

in Figure 2. The oxidation rate of copper and iron are highly dependent on the oxygen concentration, and thus a high air feed rate is recommended in order to reduce the size of the reactor. On the other hand, the nickel oxidation is less sensitive to oxygen, and hence a large sector is required to sufficiently re-oxidize the OC.

The usage of the dense support layer is critical to the thermal stability of the reactor during repeated cycles [14]: the dense layer acts as a heat reservoir to temporarily store energy from the exothermic oxidation, redistribute heat within the solid wheel, heat up the flow, and sustain the endothermic reduction. Boron nitride (BN) is used as the support material for the dense layer owing to its key properties, such as high thermal conductivity, low thermal expansion, and high chemical stability in an oxidizing environment. To select the thickness ( $\delta_{\text{bulk}}$ ) of the support layer, we can estimate the maximum temperature fluctuation ( $\Delta T_{\text{max}}$ ) by matching the thermal inertia to the exothermic heat release from the metal oxidation in the OC layer:

$$\rho_{\text{bulk}} \delta_{\text{bulk}} c_{\text{bulk}} \Delta T_{\text{max}} = \frac{\Delta h_r \rho_{\text{oc}} \delta_{\text{oc}} R_{\text{oc}} \Delta X}{v M_{\text{O}}} \quad (3)$$

where  $\rho_{\text{bulk}}$ ,  $c_{\text{bulk}}$  are the density and specific heat of the bulk layer,  $M_{\text{O}}$  is the atomic weight of oxygen,  $\Delta X$  is the range of the OC conversion utilized for reaction,  $\rho_{\text{oc}}$  and  $R_{\text{oc}}$  are the density and oxygen transport capacity,  $\Delta h_r$  is the enthalpy of the exothermic reaction. With  $\delta_{\text{bulk}}$  of about 200  $\mu\text{m}$ , the maximum temperature variation ( $\Delta T_{\text{max}}$ ) is constrained below 50K for all the OCs (assuming  $\Delta X \sim 30\%$ ).

### ***Reactor Design and Selection of Operating Conditions***

In this study, squared-shaped channels are used for all three designs. As pointed out in Part 1, the channel width should be large enough to accommodate both layers of the solid and mitigate convective cooling near the inlet. On the other hand, the channel width is constrained below a certain value to reduce the external mass diffusion resistance. On the basis of the reaction kinetics, a channel width of 2 mm is used, and hence the Damköhler number <sup>2</sup>, i.e.,  $Da_{ex} = \tau_{ex}/\tau_r$ , is less than 0.1 for all the cases.

The reduction rate along the channel depends on the local fuel concentration, temperature and the available OC. Therefore, a detailed model, as presented in Section 3, is required to obtain an accurate profile of the fuel consumption. However, for the purpose of design and comparison, an ideal scenario assuming a steady-state isothermal reactive flow with sufficient OCs along the channel can be solved analytically to approximate the fuel conversion in the reactor. The methane conversion ( $x_{CH_4}$ ) versus the channel height ( $z$ ) can be calculated as (see Appendix A):

$$\int_{y_0}^{y(z)} \frac{\zeta^n d\zeta}{(1-\zeta)^n} = \frac{P_c \delta_{oc} \varepsilon_{oc} k_p C_{tot}^{n-1} z}{2^{n-1} A_p u_0 (2x_{CH_4,0} + 1)}, \text{ where } y = \frac{1}{2x_{CH_4} + 1} \quad (4)$$

Here  $A_p$  is the cross-section area of the channel,  $P_c$  is the channel perimeter.  $u_0$  is the feed velocity, and  $x_{CH_4,0}$  is the inlet fuel volume fraction.  $k_p$  is the Arrhenius reaction rate constant, which equals  $(P/P_0)^{-a} k_0 \exp(-E/R_u T)$ .  $y(z)$  is defined as  $(2x_{CH_4} + 1)^{-1}$  and at  $z = 0$ ,  $y_0$  equals  $(2x_{CH_4,0} + 1)^{-1}$ . For complete fuel conversion  $y$  equals unity.

As an example, Figure 4 shows the fuel concentration profiles along the channels for the three OCs at 1073 K and 10 atm. The fuel concentration gradually decreases along the channel for the

---

<sup>2</sup>  $\tau_{ex}$  is the characteristic time of conversion in an external-diffusion controlled process. See Part 1 for details.

three cases, with nickel consuming the fuel faster than the other two. The fuel conversion of iron is faster than copper initially; however, in the downstream, the reduction rate slows down significantly. This is because the reduction reaction of iron oxide strongly depends on the local concentration of fuel (reaction order above unity). Thus, the integral on the left hand side of Eq. (4) diverges as the fuel concentration drops to zero, and as a result, the complete conversion of fuel is not reached at finite reactor height. In contrast, for nickel or copper, the fuel fraction decreases to zero at a finite height ( $z_{100\%}$ ).

The reactor height required to consume 99.0% of the fuel,  $z_{99\%}$ , can be calculated according to Eq.(4). Figure 5 shows  $z_{99\%}$  for all the OCs with varying inlet fuel concentration ( $x_{CH_4,0}$ ). As seen in Figure 5, a higher temperature significantly reduces  $z_{99\%}$ . Nickel has the shortest  $z_{99\%}$  because of its fast reduction rate with methane. For copper or nickel,  $z_{99\%}$  increases monotonically with the rise of  $x_{CH_4,0}$ . Thus,  $x_{CH_4,0}$  should be maintained below a certain level for nickel- (e.g., 20%~30%) and copper-based designs (e.g., 10%~20%). In contrast,  $z_{99\%}$  for iron shows a bell-shaped curve:  $z_{99\%}$  is large when  $x_{CH_4,0}$  is either very low or very high. This is again due to the fact that the reduction of iron oxide is highly sensitive to the local fuel concentration. Therefore, for iron-based designs, a high feed concentration is preferred (e.g., 40%~50%).

Figure 6 shows  $z_{99\%}$  as a function of the inlet gas velocity  $u_0$  at fixed fuel feed rates. For nickel, the predicted  $z_{99\%}$ 's are similar with each other, and they are relatively small (below 1.0m). Thus a high fuel feed rate is used for the nickel-based design. For copper, on the other hand, a significant raise of  $z_{99\%}$  is observed at high feed rate and thus the lowest fuel flow rate is adapted to reduce the channel height. The curves in the iron case show a “cross-over” pattern: at low inlet

velocity  $z_{99\%}$  increases with increasing fuel rate, while at high velocity the opposite trend is observed. Two flow rates, 2.0 and 5.0 mol m<sup>-2</sup>s<sup>-1</sup>, require a similar height for conversion at low inlet velocity. Thus, the intermediate fuel flow rate is selected for the iron-based design.

Combining the results in Figure 3, Figure 5 and Figure 6, the inlet fuel molar fraction ( $x_{CH_4,0}$ ) for copper-, nickel-, and iron-based designs are selected to be 15%, 25%, and 50%, as listed in Table 2. The reasonable inlet velocity ( $u_{fuel}$ ) is 0.09 m/s for copper, 0.25 m/s for nickel, and 0.065m/s for iron. The reactor heights are then selected accordingly, to be 0.75m, 1.00m, and 1.50m for nickel, copper, and iron, respectively.

The steam purge velocity ( $u_{fuel,p}$ ) in the fuel purge sector should be similar to  $u_{fuel}$  to completely oxidize the residual fuel. As the channel moves to the fuel purge sector, the purging steam at the inlet lowers the fuel concentration. As a result, for copper or nickel as OC, a slightly faster purging stream velocity (as compared to the fuel flow velocity) can be used owing to the monotonic relationship between  $z_{99\%}$  and  $x_{CH_4,0}$  as showed in Figure 5. For the iron case, however,  $u_{fuel,p}$  should be slower than  $u_{fuel}$  since  $z_{99\%}$  moves backwards along the curve to a much higher value as the concentration decreases. As listed in Table 2,  $u_{fuel,p}$  is 0.11m/s, 0.3m/s, 0.06m/s for the copper-, nickel-, and iron-based designs, respectively.

To separate the residual CO<sub>2</sub>, the residence time ( $\tau_{fuel,p}$ ) of a channel in the fuel purge sector is then selected to be slightly longer than the steam residence time through the channel ( $t_{fuel,p}$ ). As listed in Table 2,  $\tau_{fuel,p}$  is 6s, 2s and 15s for copper, nickel, and iron. Here it is obvious that owing to the high sensitivity of reduction to the fuel concentration, the fuel purge sector in the iron-

based design takes a larger share compared to nickel and copper. On the other hand, the purge velocity in the air purge sector ( $u_{\text{air,p}}$ ) can be much higher owing to the absence of conversion requirement, and therefore, the channel residence time ( $\tau_{\text{air,p}}$ ) in the air purge sector is much shorter. In this study,  $\tau_{\text{air,p}}$  is selected to be around 1s and  $u_{\text{air,p}}$  is around 1.0 m/s for all the three designs.

The channel residence time in the fuel sector ( $\tau_{\text{fuel}}$ ) is constrained to avoid complete OC reduction and that in the air sector ( $\tau_{\text{air}}$ ) should be long enough to provide sufficient re-oxidation. Figure 2 shows the conversion time of the OCs under typical conditions in the rotary reactor. As seen in Figure 2, the reduction of copper oxide is relatively fast, and a complete reduction is achieved after 20s. In contrast, it takes a much longer time for nickel- or iron-based OC to be fully reduced. However, the reduction rate drops significantly as NiO or Fe<sub>2</sub>O<sub>3</sub> is reduced. Thus,  $\tau_{\text{fuel}}$  is selected to be 15s for copper-based design, and around 10s for the nickel- and iron-based designs. As seen in Figure 2, the complete oxidation of copper and iron occurs within 7s. On the other hand, the oxidation rate of nickel is much slower, and it takes about 15s to re-oxidize nickel from X=0.3 to X=0.7. Therefore,  $\tau_{\text{air}}$  of about 7s is used for copper and iron, and of about 15s for the nickel design.

With the choice of the channel residence time in each sector, a cycle period ( $\tau$ ) of 30s is selected in this study for all three OCs for the purpose of comparison. The size of each sector ( $\theta$ ) can then be obtained accordingly. The diameter of the reactor is determined to achieve the target thermal capacity. The air feed rate affects the overall heat balance and determines the exhaust stream



temperature. Thus, the air velocity,  $u_{\text{air}}$ , is selected to be 0.7 m/s, 1.0m/s, and 1.0m/s for copper, nickel, and iron, respectively.

### 3. Model Formulation

A one-dimensional model was developed previously [11] to analyze the heat and mass transfer processes within the reactor. Since the entire solid reactor shares the same angular velocity, each individual channel experiences the same sequence of events in each sector. Thus, the model focuses on the reactive flow within one channel. The pressure variation, caused by laminar skin friction, is negligible [14], and a constant thermodynamic pressure is assumed. The solid phase is treated with fin approximation because of the high thermal conductivity of the dense support material. The thermal radiation is neglected due to the relatively low temperature and the small channel size. The governing equations are the species, and energy conservation equations for both solid and gas phases:

$$A_p \left[ \frac{\partial (C_g x_{g,i})}{\partial t} + \frac{\partial (u C_g x_{g,i})}{\partial z} \right] = P_c \omega_i : \quad \text{Gas species (5)}$$

$$A_{oc} \frac{\partial [(1 - \varepsilon_g) C_s]}{\partial t} = P_c \omega_{oc} : \quad \text{Solid species (6)}$$

$$A_p \left[ \frac{\partial E_g}{\partial t} + \frac{\partial (u H_g)}{\partial z} \right] = -P_c Q_{gs} + \sum_i P_c \hat{h}_{s,i} \omega_i : \quad \text{Gas energy (7)}$$

$$A_s \frac{\partial E_s}{\partial t} = A_s \frac{\partial}{\partial z} \left( k_s \frac{\partial T_s}{\partial z} \right) + P_c Q_{gs} - \sum_i P_c \hat{h}_{s,i} \omega_i : \quad \text{Solid energy (8)}$$

Here  $A_p$ ,  $A_{oc}$ , and  $A_s$  are the cross-section areas of the channel, the porous OC layer, and the solid phase, respectively.  $P_c$  is the inner perimeter of channel.  $C_g$ ,  $x_{g,i}$ ,  $\omega_i$ ,  $u$ ,  $E_g$ ,  $H_g$ , and  $T_g$  are the

concentration, mole fraction, rate of reaction, velocity, energy, enthalpy, and temperature of the bulk flow.  $C_s$ ,  $\varepsilon_g$ ,  $\omega_{oc}$ ,  $E_s$ ,  $T_s$ , and  $k_s$  are the concentration, porosity, rate of reaction, energy, temperature, and thermal conductivity of the solid.  $\hat{h}_{s,i}$  is the molar enthalpy of species  $i$  produced (or consumed) in the porous layer, and  $Q_{gs}$  is the inter-phase convective heat transfer rate, calculated as,  $Q_{gs} = h_{gs} (T_g - T_s)$ . A detailed description of the model formulation and numerical solution is given in ref. [11].

Equations (5)-(8) are solved numerically using the method of lines with upwind discretization along the spatial coordinate. Eight species are included in the simulation, i.e., CH<sub>4</sub>, CO<sub>2</sub>, H<sub>2</sub>O, O<sub>2</sub>, N<sub>2</sub>, metal, metal oxide, and inert binder. The thermal and transport properties of the gas mixture and the solid phase are calculated dynamically using the NIST property database [32]. The numerical simulation was tested using the isothermal reactive flow scenario as presented in Section 2. Figure 4 compares between predicted results (symbols) and analytical solutions (lines) and a perfect agreement is obtained. For each design, the above equations are integrated, following a sequence of fuel sector, fuel purge sector, air sector and air purge sector. The simulation is repeated until the reactor performances reach a periodic stationary state, i.e.,

$$\|\Delta T_s\| = \sqrt{\frac{1}{\tau H} \int_0^\tau \int_0^H [T_s(z, t + \tau) - T_s(z, t)]^2 dz dt} < 10^{-3} K \quad (9)$$

#### 4. Results

The periodic performances of the three designs are listed in Table 3. The fuel conversion efficiency ( $\eta_I$ ) and the carbon separation efficiency ( $\eta_{CO_2}$ ) are defined as:

$$\eta_I = 1 - \frac{\int_{fuel\ zone} \dot{m}_{CH_4,out} dt}{\int_{fuel\ zone} \dot{m}_{CH_4,in} dt}, \quad \eta_{CO_2} = \frac{\int_{fuel\ zone} \dot{m}_{CO_2,out} + \dot{m}_{CH_4,out} dt}{\int_{fuel\ zone} \dot{m}_{CO_2,in} + \dot{m}_{CH_4,in} dt} \quad (10)$$

where  $\dot{m}_{i,in}$  and  $\dot{m}_{i,out}$  are the mass flow rate of species  $i$  at the inlet and the exit respectively. All the fuel conversion efficiencies are above 99%. Nickel converts the fuel fastest and it takes only 0.49 m of the channel to consume 99% of the fuel. In contrast,  $z_{99\%}$  for iron is 1.44m, because of the slow reduction rate near exit where the concentration is low. The carbon separation efficiency for nickel is unity while that of the iron-based design is around 97%. The design criteria listed in Section 2 are satisfied for all three cases. The maximum temperature variation ( $\Delta T_{max}$ ) is listed in Table 3 and it indicates the extent of thermal distortion during the operation. Nickel and copper have similar  $\Delta T_{max}$ 's (around 20K) while for iron the maximum change is slightly higher.  $\Delta T_{max}$  occurs at the inlet for both copper and iron cases, while for nickel, it occurs near one-third of the channel from the inlet.

The feed and the flue streams are summarized in Table 3. The merged flue streams in the chamber downstream are steady. The gas velocities in the fuel zone for copper and iron are similar, both of which are slower than that for nickel. Copper and nickel have a similar flue gas composition in the fuel zone. In contrast,  $x_{CO_2}$  for iron is much lower since less  $CO_2$  is used as diluant in the feed stream. Nickel has the lowest purge feed rate due to the compactness of the design. As a result,  $x_{H_2O}$  for nickel is lowest among the three. For all cases, the air-fuel ratio is higher than stoichiometry. For iron, a small amount of methane leaves the reactor from the fuel zone, corresponding to slightly lower fuel conversion at the exit ( $\eta_I = 99.12\%$ ). For copper or nickel, on the other hand, fuel is completely consumed within the channel ( $x_{CH_4} = 0$ ). No methane is observed in the flue gas from the air zone, and no oxygen or nitrogen exits from the

fuel zone. Some  $\text{CO}_2$  exits the reactor from the air zone for copper or iron, leading to relatively lower separation efficiencies compared to nickel.

Figure 7a, b, and c shows the OC conversion ( $X$ ) as a function of time and axis within one cycle for the three OCs. Red indicates higher oxygen concentration in the OC while blue represents less oxygen. The gradients of the contours indicate the rates of OC conversion. For nickel and copper, the reduction rates are relatively lower at both the inlet and the exit because of the low temperature and low fuel concentration, respectively. The reduction rate is fastest near 40% of the reactor from the bottom, leading to a “blue region” during the fuel purge sector at which the lowest OC conversion is around 0.3 in both cases. In contrast, because of the strong dependence on the fuel concentration, the iron has the highest reactivity at the inlet and the lowest  $X$  is close to zero.

For oxidation, copper and iron share a similar pattern. The contours in the air sector (Figure 7b and Figure 7c) are more packed along the channel and the gradients are almost constant, although the extent of OC conversion is different along the channel owing to the different reduction rates in the previous fuel sector. As seen in Figure 7b and Figure 7c, the oxidation rates for copper and iron are highly sensitive to the oxygen concentration: as the oxygen concentration rises, the local OC is rapidly regenerated, leading to a slowly moving oxygen front, as seen in Figure 8. However, the nickel oxidation rate is much slower and less sensitive to the local oxygen concentration and hence the OC along the channel is slowly regenerated back to its initial state. As a result, the nickel-based design takes a larger share of the air sector, and the OC conversion patterns are relatively symmetric between the fuel and the air sectors. Besides, the

oxidation rate drops as Ni is re-oxidized, leading to a much longer oxidation time required to further regenerate the residual metallic nickel in the OC layer. Consequently, as pointed out in Section 2, not all Ni is re-oxidized at the end of the air sector (Figure 7d). In contrast, for copper or iron, the majority of the OC is regenerated before the new cycle.

Figure 7d shows the minimum OC conversion ( $X_{\min}$ ) within one cycle. For all three cases, the minimum conversion is reached at the end of the fuel purge sector. The conversion profiles are a bell-shaped curve for nickel and copper, with a minimum of 0.30 at around 40% of the height from bottom. Thus, at least 30% of oxygen remains within the OC during the entire cycle, which mitigates the carbon deposition risk [1, 31]. In contrast, the iron case has a monotonic shape of  $X_{\min}$ , with the lowest OC conversion close to zero at the inlet. The profiles of  $X_{\min}$  in Figure 7d provide additional insight to the selection of the OC thickness within the reactor, and for an optimized design, a non-uniform coating could be an interesting option. Figure 7d also shows the maximum OC conversion  $X_{\max}$  for nickel. For iron or copper,  $X_{\max}$  is close to unity along the channel. The region surrounded by  $X_{\max}$  and  $X_{\min}$ , e.g., the shaded area in Figure 7d, represents the amount of oxygen that is used in the CLC rotary operation.

Comparing the redox processes for each design, we can conclude that the limiting steps for nickel, copper, and iron are oxidation in the air sector, reduction in the fuel sector, and conversion of the residual fuel near the exit of the reactor and in the purge sector, respectively.

Figure 8 shows the molar fraction of fuel and oxygen inside the channel within one cycle. In the fuel sector, the methane concentration decreases gradually from inlet to exit. Near the outlet, the

methane concentration is zero all the time, indicating high fuel conversion efficiency for all cases. The  $\text{CH}_4$  concentration remains relatively stable in the fuel sector. The contours shift slightly upwards in panels a and c, since for nickel or iron the reduction rate decreases as the OC is reduced (Eq. (1)). In contrast, the concentration stays constant for copper case after the initial several seconds during which the flow field becomes fully developed. In the following purge sector, the contours are further stretched, because of the higher purge rates used in the nickel- or copper-based cases, and a much slower reduction rate of iron in the fuel purge sector, respectively. As the channel moves into the air sector, a slowly moving front of oxygen is observed in panels b and c, which corresponds to the rapid re-oxidization of OC and hence fast oxygen consumption, as mentioned before. Behind the front, the OC is fully regenerated, and the flow remains stable for the rest of the stay in the air sector (see Figure 9b). In contrast, the profiles for nickel vary mildly, leading to a quasi-steady flow field in the air sector (Figure 9a). As the channel travels to the air purge sector, the residual air is removed and the oxygen concentration quickly drops to zero.

Figure 9 shows the flow velocity in the channel. Light colors correspond to low velocities. In the nickel design (panel a), the flow remains stable for the majority of the period, and only minor transitions are observed at the beginning of the fuel and the fuel purge sectors. In contrast, the transition periods for the iron-based design are long and strong variations are observed at the beginning of all the sectors. The copper case exhibits an intermediate behavior, which has a clear steady state in the late fuel and air sectors, and also strong oscillations in the fuel purge sector and at the beginning of the air sector. Fluid velocity variations in the reactor cause pressure fluctuations, gas leakage between adjacent sectors, and mechanical stresses inside the reactor.

From this perspective, nickel-based design merits over the other two because of its relatively stable and mildly varying flow fields throughout different sectors.

Figure 10 shows the fuel conversion throughout the channel. Here, the conversion of fuel,  $\eta_I$ , as a function of axis,  $z$ , is calculated as [33],

$$\eta_I(z) = 1 - \tilde{C}_{CH_4, fuel}(z) - \tilde{C}_{CH_4, fuel\ purge}(z) \quad (11)$$

Here  $\tilde{C}_{CH_4}$  is the normalized  $CH_4$  flux, defined as  $\bar{m}_{CH_4}(z)/\dot{m}_{CH_4, inlet}$  with  $\bar{m}_{CH_4}(z)$  being the time-averaged methane flow rate at  $z$  and  $\dot{m}_{CH_4, inlet}$  the inlet feed rate. The majority of methane is consumed within the fuel sector while a small fraction (6% for nickel, 18% for copper, and 29% for iron) is carried over to the following fuel-purge sector and then oxidized by the OC. As seen in Figure 10, almost all methane is converted within 75% of the channel for all the three designs, i.e., 0.56m, 0.75m, and 1.13m for nickel, copper, and iron, respectively. The rest 25% of the reactor accounts for uncertainties and maintains stable operations under off-design conditions. As seen in panels a and b, nickel and copper share a similar conversion pattern: the overall conversion efficiency rises quickly near the inlet, but the increase slows down as it approaches the exit. The inflection point of the curve corresponds to the position with the fastest reactivity, as observed in Figure 7. In contrast, iron has a different pattern: the overall efficiency increases convexly; the methane concentration in the fuel-purge sector exhibits an asymmetric bell-shaped curve with a fat tail near the exit. This is again due to the fact that reduction of iron strongly depends on the local fuel concentration and hence as the majority of the fuel is consumed near the exit, the reduction rate drops significantly. Thus, to reach high fuel conversion efficiency, a sufficient redundant height is required for iron to account for the tail effect.

The temperature distribution within the channel is critical to the redox reactivities and the operational stability. Figure 11 compares the time-averaged temperature distribution of the solid and gas phases. For all the three OCs, the solid temperature rises monotonically from the inlet to the exit. The temperature of copper is slightly lower than nickel or iron, owing to the material limitation, as seen in panel b. The gas temperature is dominated by the solid except at the inlet where the feed stream is much cooler. As seen in Figure 11,  $\Delta T_{\max}$  is around 20K for copper or nickel and about 35K for iron. For iron or copper,  $\Delta T_{\max}$  occurs at the inlet while for nickel it occurs around 1/3 of the channel from bottom, as also listed in Table 3.

Figure 12 shows the solid temperature deviation from its time-averaged temperature along the channel within one cycle. Blue colors correspond to temperature drops and red correspond to rises. As seen in panels a and c, solid temperature decreases in the fuel sector because of the convective cooling as well as the endothermic reduction reactions. In the copper case, however, the heat release from the exothermic reduction balances the cooling effect, and hence the solid temperature remains almost constant within the fuel sector. In all cases, the solid temperature jumps quickly in the air sector where the highly exothermic oxidation rapidly heats up the solid phase back to its initial state. As seen in panels b and c, the solid temperature fluctuation for copper or iron is small within the majority of the reactor and large changes are only observed near the inlet, as also seen in Figure 11. In contrast, strong variations are observed within the bottom half of the reactor in the nickel case. Nevertheless, for all three cases,  $\Delta T_{\max}$  is small, and thus the thermal stresses are limited.



Sensitivity analysis is also performed to identify the key parameters and provide information on the design robustness. The sensitivity ( $\tilde{S}_{\chi \rightarrow \psi}$ ) of an output ( $\psi$ ) to an input ( $\chi$ ) is defined as:

$$\tilde{S}_{\chi \rightarrow \psi} = \frac{\partial \ln \psi}{\partial \ln \chi} \approx \frac{\chi}{\psi} \frac{\Delta \psi}{\Delta \chi} \quad (12)$$

For the rotary CLC design, the most important outputs are [14]: the fuel conversion ( $z_{95\%}$ ), the carbon separation efficiency ( $\eta_{CO_2}$ ), and the maximum solid temperature fluctuation ( $\Delta T_{max}$ ). Input parameters are grouped into three types [14, 34]: the OC kinetics, the design configurations, and the operating conditions. The model is run repeatedly with each input parameter changed by a certain range (e.g., -10%, -5%, +5%, and +10%) from its base value. The sensitivity of  $z_{95\%}$ ,  $\eta_{CO_2}$  and  $\Delta T_{max}$  are shown in Figure 13, Figure 14 and Figure 16 respectively. Parameters that result in very small changes of output are omitted for clarity.

Figure 13 shows the sensitivity of  $z_{95\%}$ . For all the OCs,  $z_{95\%}$  is most sensitive to the reduction kinetics, the inlet temperature and the operating pressure. With lower reduction rates, the temperature drops significantly which further decreases the reactivity. Thus, a much longer distance is required for fuel conversion. Similarly, as the operating pressure increases or the inlet temperature drops, the stronger convective cooling effects lower the solid temperature, leading to reduced reduction rates. The sensitivities for copper are generally higher than the other two, while the iron case is most robust with varying designs and operating conditions. The oxidation kinetics is less important for copper or iron. However,  $z_{95\%}$  of the nickel case is sensitive to the oxidation kinetics, because the extent of the OC conversion at the end of the air sector strongly depends on the oxidation rate. For each parameter showed in Figure 13, the three OC cases have

the same sign of sensitivity, and therefore, the effects of each input on the fuel conversion are similar for the three designs.

Figure 14 shows the sensitivity of  $\eta_{CO_2}$ . As seen in Figure 14,  $\eta_{CO_2}$  can be significantly improved by using a shorter channel, a faster purging rate or simply a longer purging time. For nickel, the sensitivities are all close to zero, due to a sufficient purging applied in the base case. By raising the inlet temperature, an increase of  $\eta_{CO_2}$  is observed for copper in that  $z_{95\%}$  shifts significantly backwards to the inlet, as seen in Figure 13, which leads to a significant solid temperature increase and hence a much higher gas velocity near the inlet. In contrast, the opposite trend is observed for iron, because in this case  $z_{95\%}$  changes only mildly, and thus the velocity increase near the inlet is small. Meanwhile, owing to a lower methane feed rate at the raised inlet temperature, less product molecules are generated from the reduction reaction, and hence the velocity decreases near the exit where the majority of the fuel is oxidized. This is evident in Figure 15, which compares the time-averaged gas velocity in the fuel purge sector for copper (panel a) and iron (panel b) at different inlet temperatures. For both cases, the velocity near the exit decreases with the increase of the inlet temperature. For copper, however, a relative large velocity increase is observed within the bottom half of the reactor, which greatly shortens the gas residence time, and hence leads to a higher  $\eta_{CO_2}$ .

Figure 16 shows that  $\Delta T_{max}$  is most sensitive to the reduction kinetics, pressure and the inlet temperature. As the reduction rate increases, more OC is consumed in the fuel sector, leading to higher energy release in the following air sector, and thus a larger temperature variation. In contrast, a higher pressure or a lower feed temperature inhibits the redox rate and thus decreases

$\Delta T_{max}$ . Similarly, the sensitivities of  $\Delta T_{max}$  are strongest for copper, followed by nickel, while the iron-based design is the most robust. For most of the input parameters, similar responses of  $\Delta T_{max}$  are recorded for the three cases. One exception is that as the thickness of the solid layer ( $\delta_{bulk}$ ) increases,  $\Delta T_{max}$  decreases for nickel and iron because of the higher thermal inertia of the solid phase. On the other hand, a larger temperature variation is observed for copper. This is because the conductive heat transfer in the solid phase is also enhanced by a thicker solid layer. The chemical energy absorbed in the solid phase is more effectively transferred to the inlet, which raises the surface temperature. Thus, the enhanced reaction rate consumes more OC in the fuel sector, which leads to a larger temperature fluctuation near the inlet.

## 5. Discussion

As discussed in the sensitivity analysis, the OC kinetics, the inlet temperatures and the operating pressures are the most important parameters in determining the periodic performances of the rotary CLC reactor. From Eq.(1), different operating pressures or inlet temperatures can significantly affect the reaction rates by changing the fuel concentration or altering pressure inhibition effects. In addition, a raised operating pressure or a reduced inlet temperature enhances the cooling effect and decreases the reactivity. Besides, different operating conditions alter the flow field, change the gas residence time, and greatly affect the carbon separation efficiency. Thus, in order to utilize the rotary reactor in a power generation system, it is necessary to understand how the operating conditions in a power cycle affect the performance of the reactor, and how to adjust the design accordingly.

In general, the scaling strategy follows a similar logic to the selection of the base-case design parameters, as proposed in Part 1. However, with the results from the base case, the scaling process can be greatly simplified:

- I. The heat duty of the stream is kept to be the same as in the base case to maintain a similar temperature profile inside the reactor and provide the same flue stream temperature.*
- II. The fuel feed rate is selected to be constant to produce similar fuel concentration and OC conversion profiles along the channel.*
- III. The height of the reactor is adjusted accordingly to provide an adequate gas residence time for fuel conversion.*
- IV. The cycle period and the size of each sector are sufficient for OC regeneration and carbon separation.*

Panels a and b in Figure 17 compare  $z_{99\%}$  calculated according to the steady isothermal reactive flow (Eq.(4)) for varying operating pressures and inlet temperatures, respectively, following the aforementioned procedure: the inlet velocity is adjusted to maintain the heat duty the same as in the base cases; the inlet fuel molar fraction is selected to provide the same fuel feed rate. Same design parameters and operating conditions with the base cases are used. An average temperature along the channel, according to Figure 11, is selected to represent the reaction temperature.

With a higher inlet temperature, the surface temperature increases, leading to a higher reaction rate and thus a smaller  $z_{99\%}$ . On the other hand, because of the higher gas velocity and the lower fuel concentration at higher inlet temperature, the reduction rate is reduced and hence  $z_{99\%}$  increases, as seen in Figure 6. The above two effects balance and thus  $z_{99\%}$  remains almost

constant with varying inlet temperatures for the three OCs (Figure 17b). For iron,  $\eta_{99\%}$  slightly increases with a higher inlet temperature. The operating pressure influences the fuel conversion by changing the fuel concentration or altering the pressure inhibition effects, as discussed in Section 2. The combined effect depends on the relative importance of these two factors (Figure 17a). For copper and nickel, the reduction reaction order is smaller than the pressure coefficient, and hence the inhibition effect dominates at a higher pressure. On the other hand,  $\eta_{99\%}$  decreases at elevated pressures for iron because of the stronger reactivity increase caused by the raised concentration. Nevertheless, the change of  $\eta_{99\%}$  with varying pressures is small, especially for the nickel-based design, and thus in an industrial application, a sufficient redundant height can be used to account for the pressure effect.

Table 4 lists the design parameters and the operating conditions at a low (5atm) and a high pressure (20atm). The design follows the aforementioned scaling strategies. The performance of each design is tested using the model presented in Section 3, and the simulated results are listed in Table 4. According to Figure 17a, a shorter reactor height is used for the low pressure operation with copper and nickel, while a longer reactor is selected to account for the reduced reduction rate of iron at 5 atm. The cycle period is adjusted at different pressures to match the residence time of gas with that of the channel, and account for the changes of the flow field and the channel height. The sizes of sectors are similar to the base cases with minor revisions for copper and iron to ensure sufficient purging, adequate OC regeneration, and avoid the complete OC reduction. For all the designs showed in Table 4, the conversion efficiencies are close to unity and over 95% of carbon dioxide is captured. Larger temperature fluctuations are observed under higher pressures, as opposed to the trend showed in Figure 16, because of the longer

reduction period applied at high pressure. As a result, more OC is consumed, as seen in Figure 18, leading to a larger temperature rise in the following air sector. The convective cooling effect is less important as compared to the sensitivity study (Figure 16), because of the similar heating load of the streams. Thus, similar solid temperature profiles are observed, as plotted in Figure 18, although a higher pressure slightly lowers the temperature and decreases the surface reactivity. As a result, the change of  $\eta_{99\%}$  with respect to the base case is larger than that predicted by Eq.(4).

Table 5 compares the designs and the operating conditions with different inlet temperatures. The reactor heights are the same as in the base cases, and the flow velocities are adjusted to account for the change of the temperature ranges from the inlet to the exit. The fuel molar fraction at the inlet is varied accordingly to maintain a constant feed rate. A same cycle period is used, since the change of the gas residence time is small. For all the cases, the conversion efficiencies are close to unity, and over 95% of  $\text{CO}_2$  is captured.  $\Delta T_{max}$  decreases at higher inlet temperatures, as against to the trends observed in Figure 16. This is because following the above scaling procedure the fuel concentration at the inlet inversely changes with the inlet temperature. Therefore, with a higher flow velocity at higher inlet temperatures the fuel concentration spans more uniformly throughout the reactor and hence the OC conversion along the channel is more uniform, as seen in Figure 19. As a result, the chemical energy released along the channel is uniform under high inlet temperatures, and hence, the temperature fluctuation is small.

## 6. Conclusion

In this work, the idea of a rotary reactor with micro-channels to conduct CLC was extended to the utilization of three different OCs, i.e., copper, nickel, and iron. The reactor designs and the

operating conditions follow the design procedures proposed in Part 1. The reaction mechanisms used were based on the one-step overall kinetics proposed by Abad and co-workers [15-17] covering a wide range of conditions. The reactivities of different OCs with methane and air were analyzed and compared, and the effect of the reaction rates on the choice of the design was discussed. Because of the fast reduction rate, a higher fuel feed rate can be used for nickel and hence a shorter reactor can adequately consume the fuel. In contrast, the oxidation rate of nickel is slow, and thus, a large share of air sector is required to sufficiently regenerate the OC inside the channel. For the copper design, because of the relative lower operating temperature, and the less metal oxide loading in the OC, a lower fuel feed rate is preferred. The design of copper is mainly controlled by the fuel conversion in the fuel sector. For the iron-based design, the reduction rate strongly depends on the fuel concentration, and therefore, a high fuel concentration at the inlet is selected to effectively improve the conversion rate. Due to the rapid drop of the reduction rate with the decrease of the fuel concentration, a sufficient redundant height is used for the iron-based design to provide an adequate gas residence time in the fuel and the fuel purge sectors to reach the desirable fuel conversion efficiency. Thus, the fuel purge sector in the iron-based design usually takes a large share to ensure carbon separation.

The one-dimensional reactive plug-flow model developed in the previous studies was adapted to evaluate the performances of the reactor designs with the three OCs. Based on the operating conditions selected, the nickel has the smallest dimensions, while the iron-based design is largest. For all the cases, complete fuel conversion and carbon separation efficiencies are obtained and reasonable operational stability is maintained. The simulation validated that the nickel-based design is mainly limited by oxidation, while the iron-based design is controlled by the low

reduction rate, especially in the fuel purge sector. In the periodic states, the gas temperature increases monotonically, and it is mainly determined by the solid temperature. The temperature fluctuations with time are small for all the cases, and hence the thermal-stress-induced fracture is limited. Sensitivity tests showed that the OC kinetics, the operating pressure and the inlet temperature are the most important factors. Copper-based design is most sensitive to the varying input parameters while iron case is most robust. Scaling strategies were also proposed to up-scale the design to different pressures and inlet temperatures. The simulations showed that the design can be easily adapted to different conditions to produce satisfactory periodic performance with reasonable stability. The parametric study and the numerical simulation under different conditions validate the design procedures proposed in Part 1.

## **Acknowledgement**

This study is financially supported by a grant from the MASDAR Institute of Science and Technology and the King Abdullah University of Science and Technology (KAUST) Investigator Award.



## Reference

- [1] J. Adanez, A. Abad, F. Garcia-Labiano, P. Gayan, L.F. de Diego, Progress in Chemical-Looping Combustion and Reforming technologies, Progress in Energy and Combustion Science, 38 (2012) 215-282.
- [2] A. Lyngfelt, B. Leckner, T. Mattisson, A fluidized-bed combustion process with inherent CO<sub>2</sub> separation; application of chemical-looping combustion, Chem. Eng. Sci., 56 (2001) 3101-3113.
- [3] C. Linderholm, T. Mattisson, A. Lyngfelt, Long-term integrity testing of spray-dried particles in a 10-kW chemical-looping combustor using natural gas as fuel, Fuel, 88 (2009) 2083-2096.
- [4] J. Adanez, P. Gayan, J. Celaya, L.F. de Diego, F. Garcia-Labiano, A. Abad, Chemical Looping Combustion in a 10 kWth Prototype Using a CuO/Al<sub>2</sub>O<sub>3</sub> Oxygen Carrier: Effect of Operating Conditions on Methane Combustion, Ind. Eng. Chem. Res., 45 (2006) 6075-6080.
- [5] T. Proell, P. Kolbitsch, J. Bolhar-Nordenkamp, H. Hofbauer, A novel dual circulating fluidized bed system for chemical looping processes, AIChE J., 55 (2009) 3255-3266.
- [6] N. Berguerand, A. Lyngfelt, Operation in a 10 kWth chemical-looping combustor for solid fuel-testing with a Mexican petroleum coke, Energy Procedia, 1 (2009) 407-414.
- [7] L. Shen, J. Wu, Z. Gao, J. Xiao, Characterization of chemical looping combustion of coal in a 1 kWth reactor with a nickel-based oxygen carrier, Combust. Flame, 157 (2010) 934-942.
- [8] D. Pavone, CO<sub>2</sub> capture by means of chemical looping combustion., in: Proceedings of the COMSOL Multiphysics User's Conference., Paris, France, 2005.
- [9] D. Pavone, M. Rolland, E. Lebas, CO<sub>2</sub> capture using chemical looping combustion for gas turbine application., in: Proceedings of 8th International Conference of Greenhouse Gas Control Technologies (GHGT-8). Trondheim, Norway, 2006.

- [10] J.E. Cichanowicz, L.J. Muzio, Rotary regenerative chemical looping combustion. Patent US 2009/0265978, in, USA . 2009, pp. 9pp.
- [11] Z. Zhao, T. Chen, A.F. Ghoniem, Rotary Bed Reactor for Chemical-Looping Combustion with Carbon Capture. Part 1: Reactor Design and Model Development, *Energy & Fuels*, 27 (2013) 327-343.
- [12] Z. Zhao, Rotary bed reactor for chemical-looping combustion with carbon capture, in: Dept. of Mechanical Engineering, Massachusetts Institute of Technology, Cambridge, 2012.
- [13] Z. Zhao, C.O. Iløje, T. Chen, A.F. Ghoniem, Design of a Rotary Reactor for Chemical-looping Combustion. Part 1: Fundamentals and Design Methodology, Submitted to *Fuel* for publication, (2013).
- [14] Z. Zhao, T. Chen, A.F. Ghoniem, Rotary Bed Reactor for Chemical-Looping Combustion with Carbon Capture. Part 2: Base Case and Sensitivity Analysis, *Energy & Fuels*, 27 (2013) 344-359.
- [15] A. Abad, J. Adanez, F. Garcia-Labiano, D.L.F. de, P. Gayan, J. Celaya, Mapping of the range of operational conditions for Cu-, Fe-, and Ni-based oxygen carriers in chemical-looping combustion, *Chem. Eng. Sci.*, 62 (2007) 533-549.
- [16] F. Garcia-Labiano, J. Adanez, L.F. de Diego, P. Gayan, A. Abad, Effect of Pressure on the Behavior of Copper-, Iron-, and Nickel-Based Oxygen Carriers for Chemical-Looping Combustion, *Energy Fuels*, 20 (2006) 26-33.
- [17] F. Garcia-Labiano, L.F. de Diego, J. Adanez, A. Abad, P. Gayan, Reduction and Oxidation Kinetics of a Copper-Based Oxygen Carrier Prepared by Impregnation for Chemical-Looping Combustion, *Ind. Eng. Chem. Res.*, 43 (2004) 8168-8177.

- [18] R. Naqvi, Analysis of Natural Gas-Fired Power Cycles with Chemical Looping Combustion for CO<sub>2</sub> Capture., in, Norwegian University of Science and Technology, 2006.
- [19] G. Energy, Heavy duty gas turbine products, GEA-12985H (06/09), General Electric, (2009).
- [20] J. Adanez, L.F. de Diego, F. Garcia-Labiano, P. Gayan, A. Abad, J.M. Palacios, Selection of Oxygen Carriers for Chemical-Looping Combustion, *Energy Fuels*, 18 (2004) 371-377.
- [21] T. Mattisson, M. Johansson, A. Lyngfelt, The use of NiO as an oxygen carrier in chemical-looping combustion, *Fuel*, 85 (2006) 736-747.
- [22] M. Johansson, T. Mattisson, A. Lyngfelt, A. Abad, Using continuous and pulse experiments to compare two promising nickel-based oxygen carriers for use in chemical-looping technologies, *Fuel*, 87 (2008) 988-1001.
- [23] P. Cho, T. Mattisson, A. Lyngfelt, Comparison of iron-, nickel-, copper- and manganese-based oxygen carriers for chemical-looping combustion, *Fuel*, 83 (2004) 1215-1225.
- [24] L.F. de Diego, F. Garcia-Labiano, J. Adanez, P. Gayan, A. Abad, B.M. Corbella, J.M. Palacios, Development of Cu-based oxygen carriers for chemical-looping combustion, *Fuel*, 83 (2004) 1749-1757.
- [25] M. Johansson, T. Mattisson, A. Lyngfelt, Investigation of Fe<sub>2</sub>O<sub>3</sub> with MgAl<sub>2</sub>O<sub>4</sub> for Chemical-Looping Combustion, *Ind. Eng. Chem. Res.*, 43 (2004) 6978-6987.
- [26] M. Ryden, E. Cleverstam, M. Johansson, A. Lyngfelt, T. Mattisson, Fe<sub>2</sub>O<sub>3</sub> on Ce-, Ca-, or Mg-stabilized ZrO<sub>2</sub> as oxygen carrier for chemical-looping combustion using NiO as additive, *AIChE J.*, 56 (2010) 2211-2220.

- [27] F. Garcia-Labiano, L.F. de Diego, J. Adanez, A. Abad, P. Gayan, Temperature variations in the oxygen carrier particles during their reduction and oxidation in a chemical-looping combustion system, *Chem. Eng. Sci.*, 60 (2005) 851-862.
- [28] R. Siriwardane, J. Poston, K. Chaudhari, A. Zinn, T. Simonyi, C. Robinson, Chemical-Looping Combustion of Simulated Synthesis Gas Using Nickel Oxide Oxygen Carrier Supported on Bentonite, *Energy Fuels*, 21 (2007) 1582-1591.
- [29] H. Jin, T. Okamoto, M. Ishida, Development of a Novel Chemical-Looping Combustion: Synthesis of a Solid Looping Material of  $\text{NiO/NiAl}_2\text{O}_4$ , *Ind. Eng. Chem. Res.*, 38 (1999) 126-132.
- [30] G. Wu, W.A. Sirignano, F.A. Williams, Simulation of transient convective burning of an n-octane droplet using a four-step reduced mechanism, *Combustion and Flame*, 158 (2011) 1171-1180.
- [31] E. Jerndal, T. Mattisson, A. Lyngfelt, Thermal analysis of chemical-looping combustion, *Chem. Eng. Res. Des.*, 84 (2006) 795-806.
- [32] NIST Standard Reference Database Number 69, [webbook.nist.gov/chemistry](http://webbook.nist.gov/chemistry), accessed 12/2011.
- [33] Z. Zhao, T. Chen, A.F. Ghoniem, Rotary Bed Reactor for Chemical-Looping Combustion with Carbon Capture. Part 2: Base Case and Sensitivity Analysis, *Energy & Fuels*, 27 (2012) 344-359.
- [34] Z. Zhao, C.O. Iloeje, T. Chen, Design of a Rotary Bed Reactor for Chemical-looping Combustion. Part 1: Fundamentals and Design Methodology, Submitted for publication, (2013).

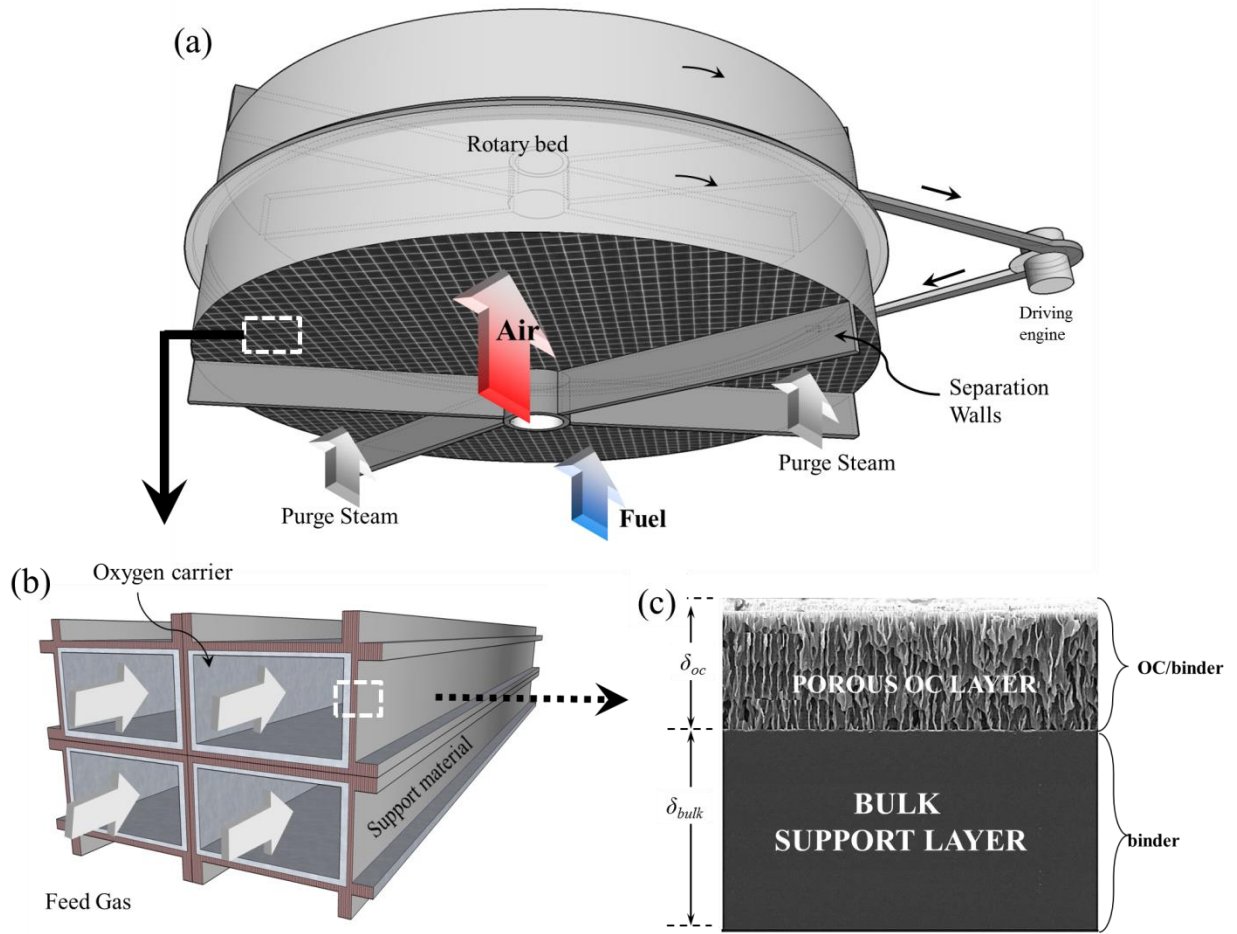


Figure 1. Schematic diagram of rotary CLC system design [11]: (a) front view, (b) bottom view of channels, and (c) the oxygen carrier coated on the channel walls.

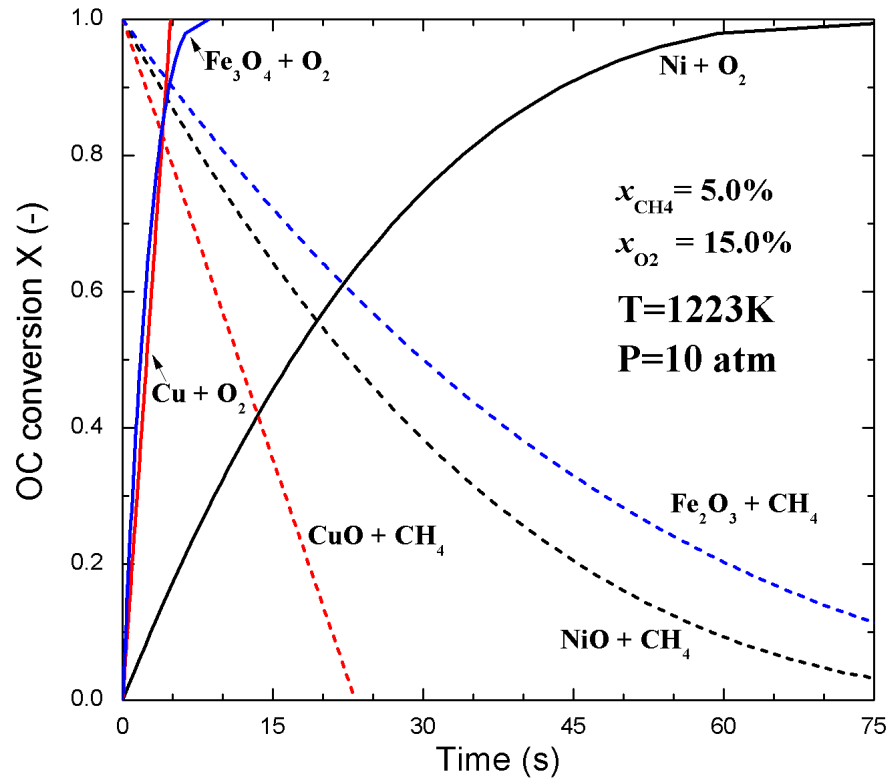


Figure 2 OC conversion versus time for reduction (dashed lines) and oxidation (solid lines). The operating conditions are similar to those in the designs.

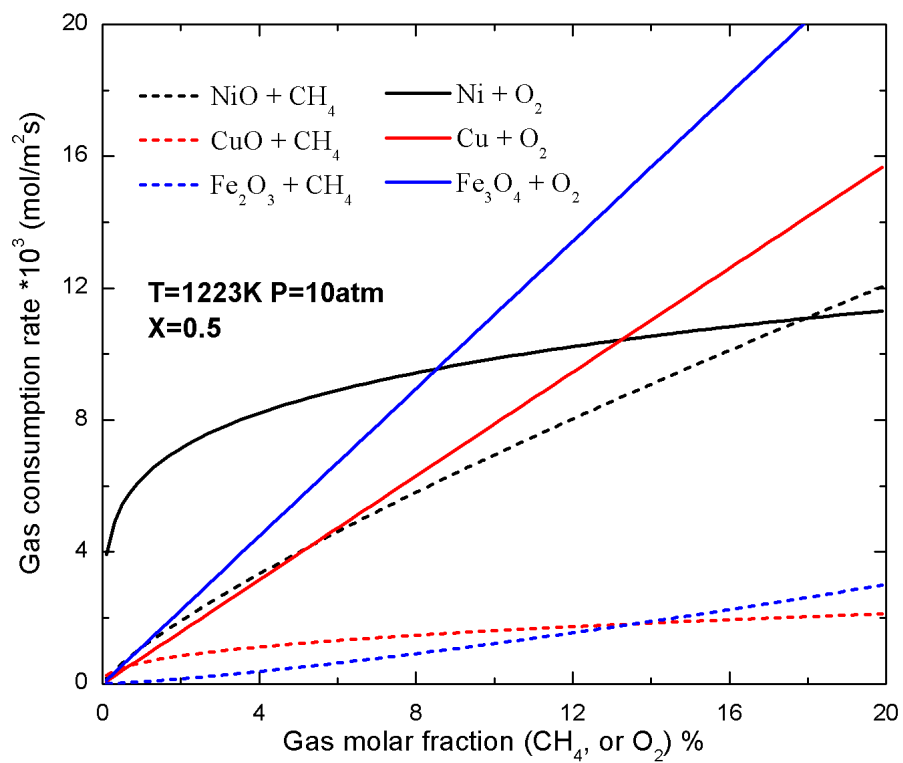


Figure 3 Gas consumption rate as a function of gas concentration for reduction (dashed lines) and oxidation (solid lines). The operating conditions are similar to those in the designs.

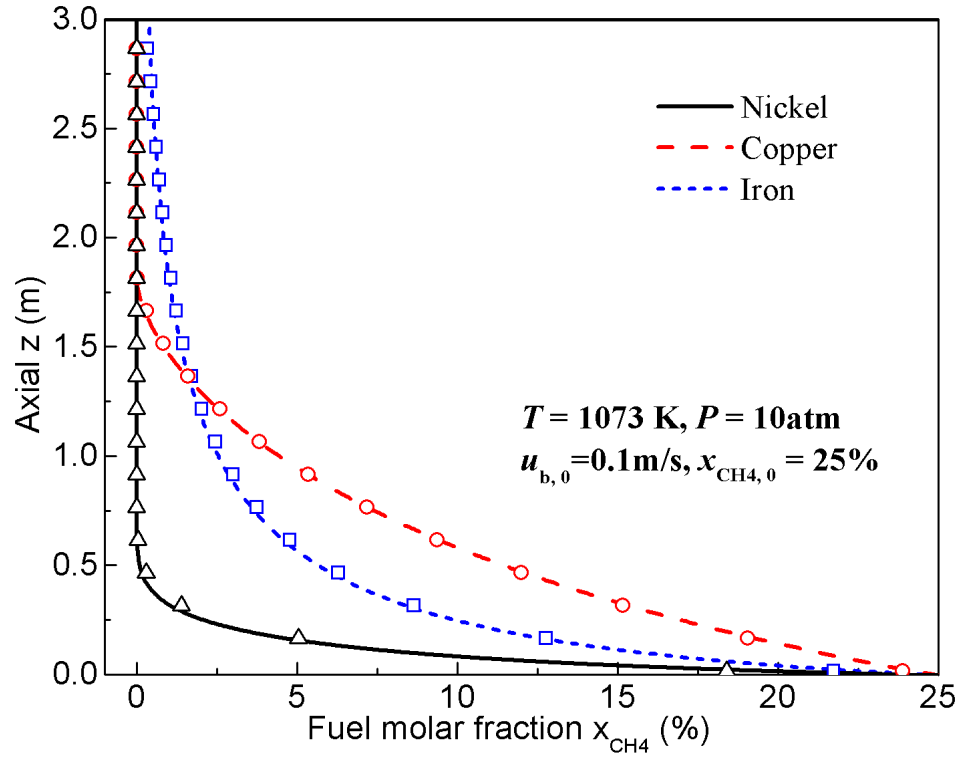


Figure 4 Comparison of fuel molar fraction profiles of different OCs along the channel for the steady-state isothermal reduction. Lines are from analytical solutions and symbols are model-simulated results.



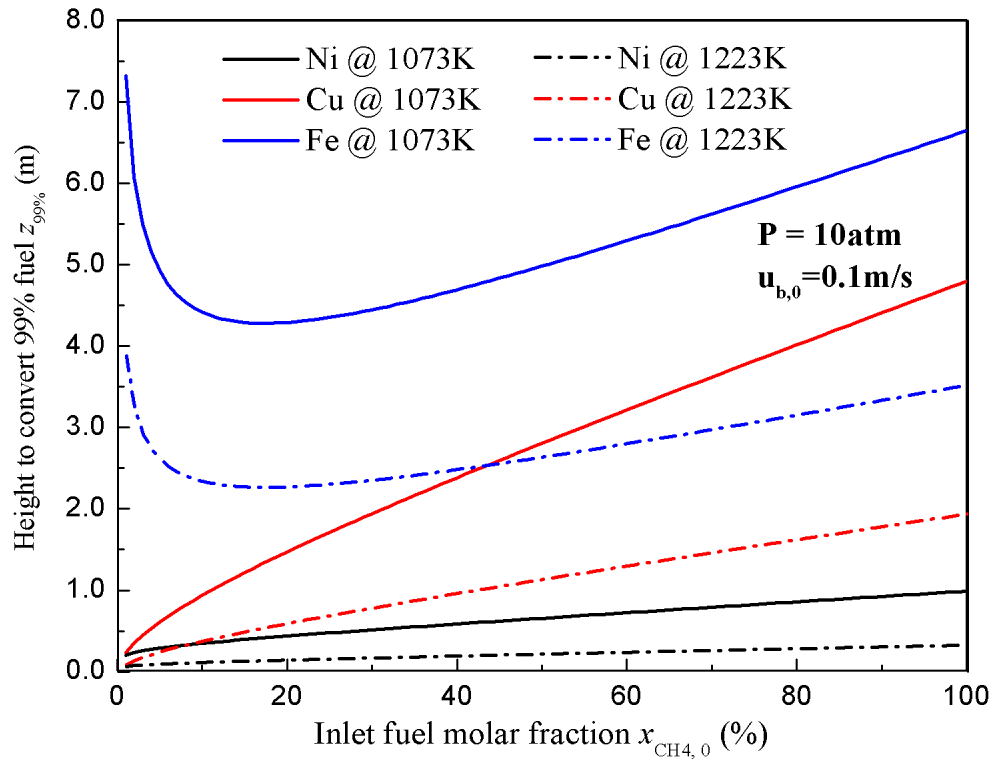


Figure 5 The channel height to reach 99.0% fuel conversion,  $z_{99\%}$ , as a function of the inlet fuel molar fraction for the three OCs at two different temperatures.

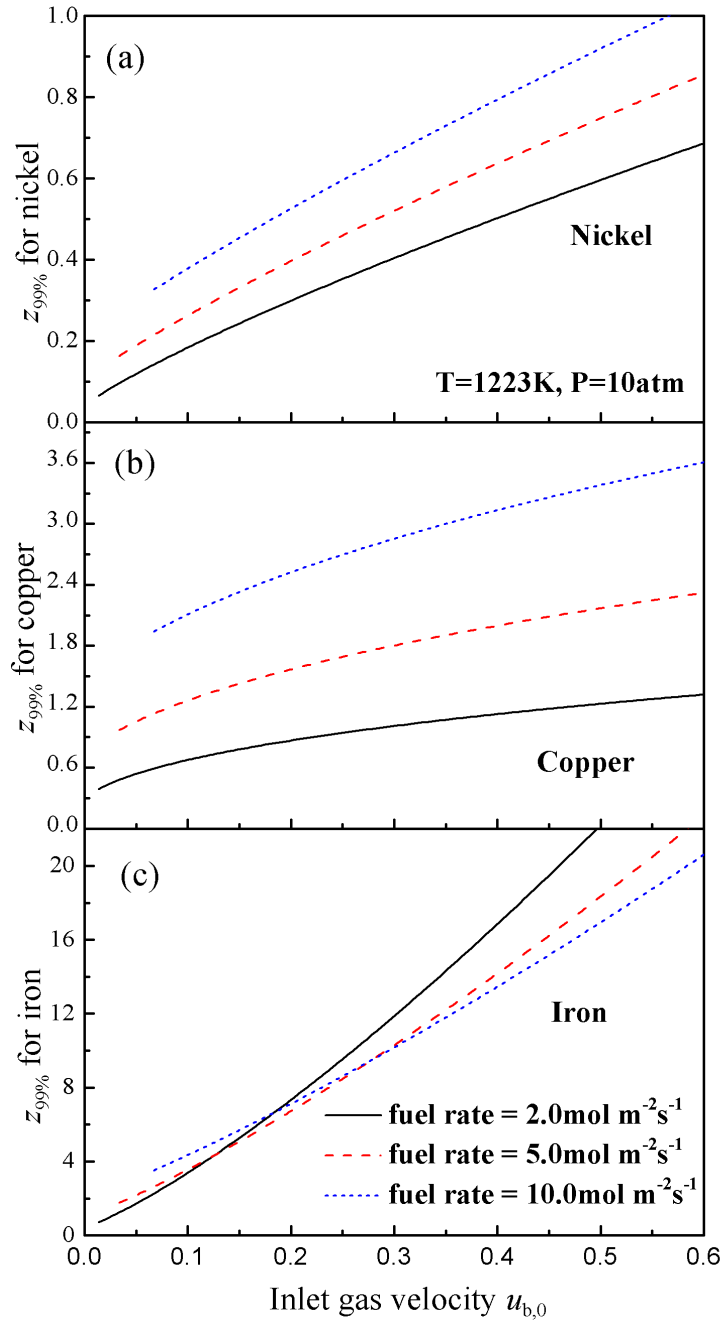


Figure 6  $z_{99\%}$  versus inlet gas velocity  $u_{b,0}$  for the three OCs at different fuel feed rate. For each curve, the inlet fuel concentration is varied accordingly to keep the fuel flow rate constant. The operating condition is 1223K and 10 atm, and the inlet velocities are evaluated at 823K.

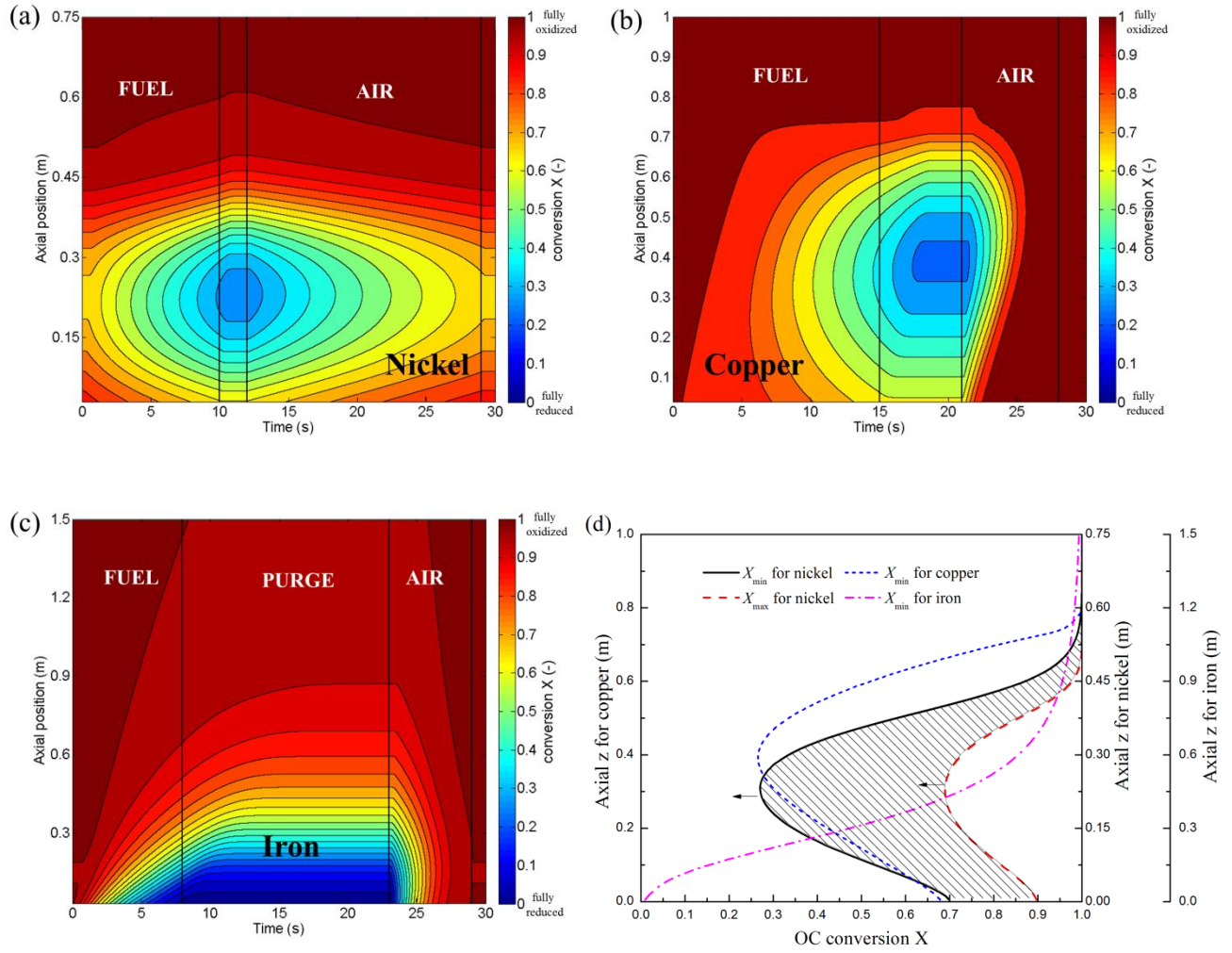


Figure 7 OC conversion versus time within one cycle for (a) nickel-, (b) copper-, and (c) iron-based designs. Panel d shows the minimum OC conversion within one cycle for the three OCs. The maximum OC conversion for nickel is also included. The shaded area in panel d represents the conversion range of nickel used in the cyclic operation.

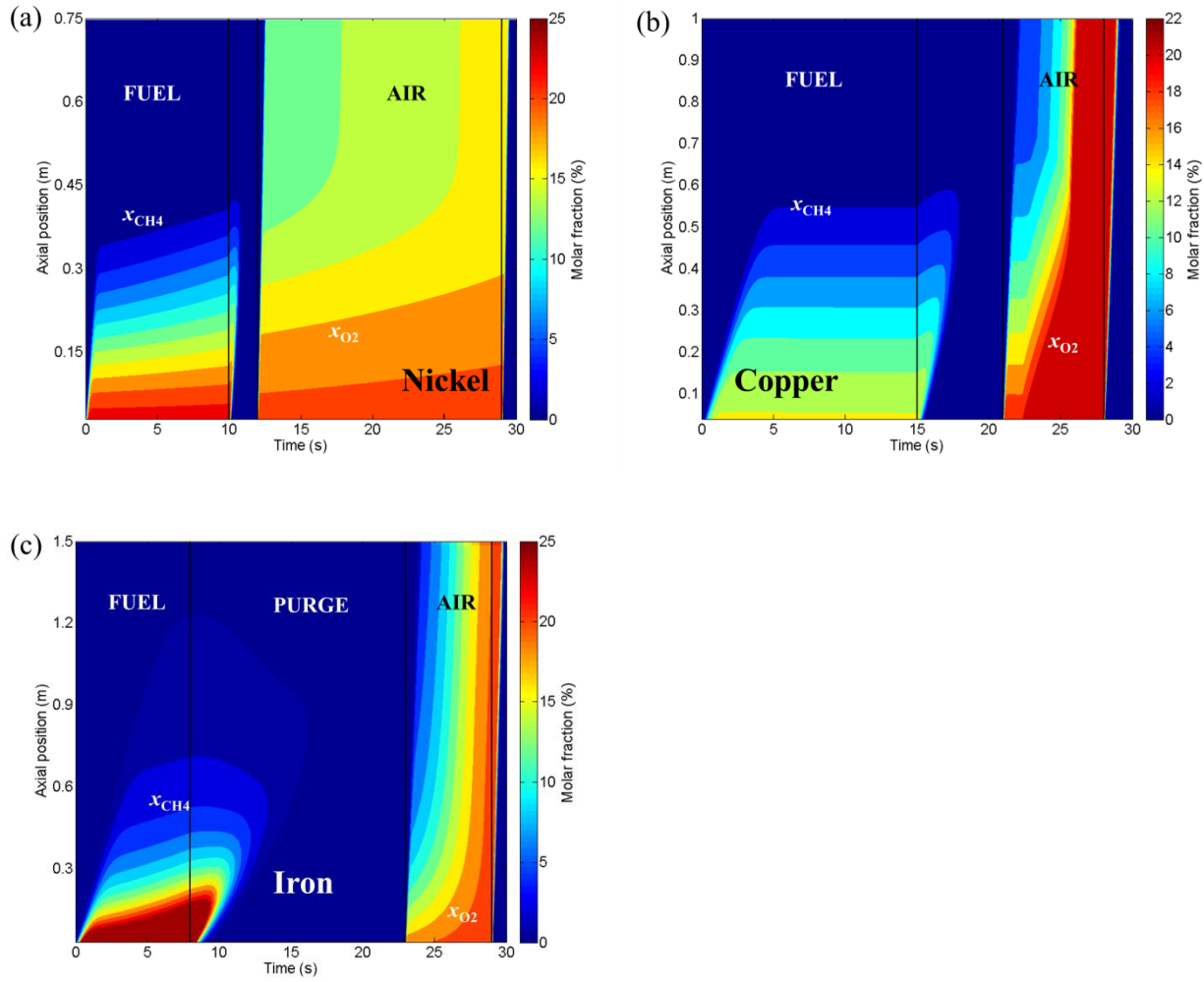


Figure 8 Molar fraction of the fuel and oxygen in one cycle for (a) nickel-, (b) copper-, and (c) iron-based designs.

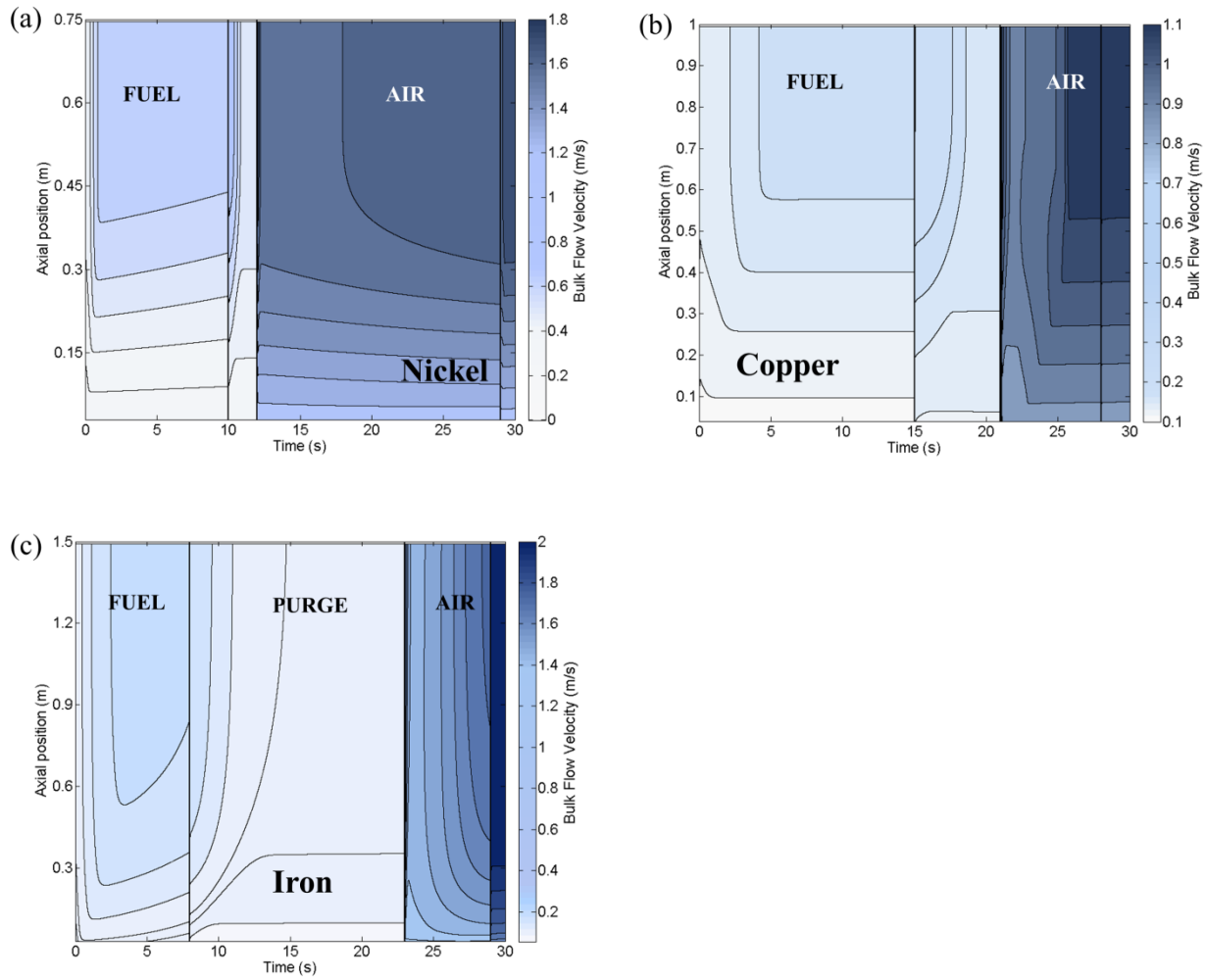


Figure 9 Bulk flow velocity versus time within one cycle for (a) nickel-, (b) copper-, and (c) iron-based designs.

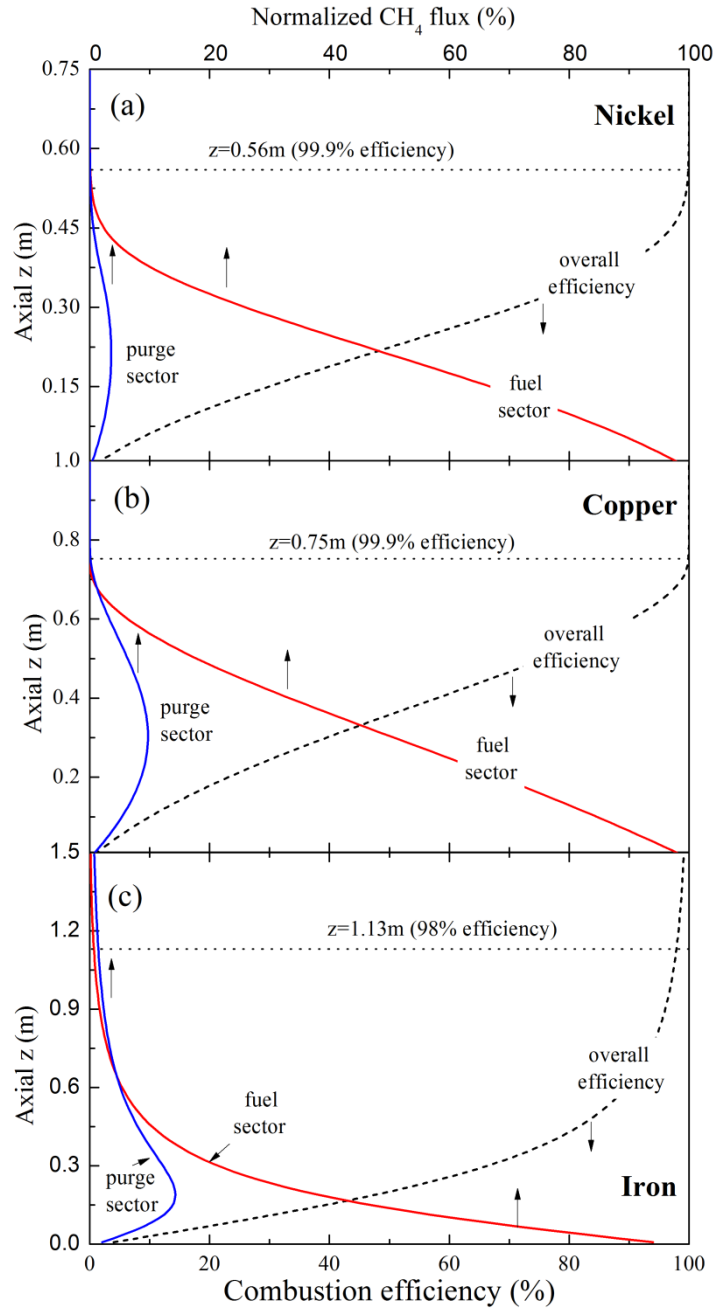


Figure 10 Normalized  $\text{CH}_4$  concentration in the fuel and purge sectors (solid lines) and the periodic fuel conversion efficiency (dashed line) as a function of the axial position for (a) nickel-, (b) copper-, and (c) iron-based designs.

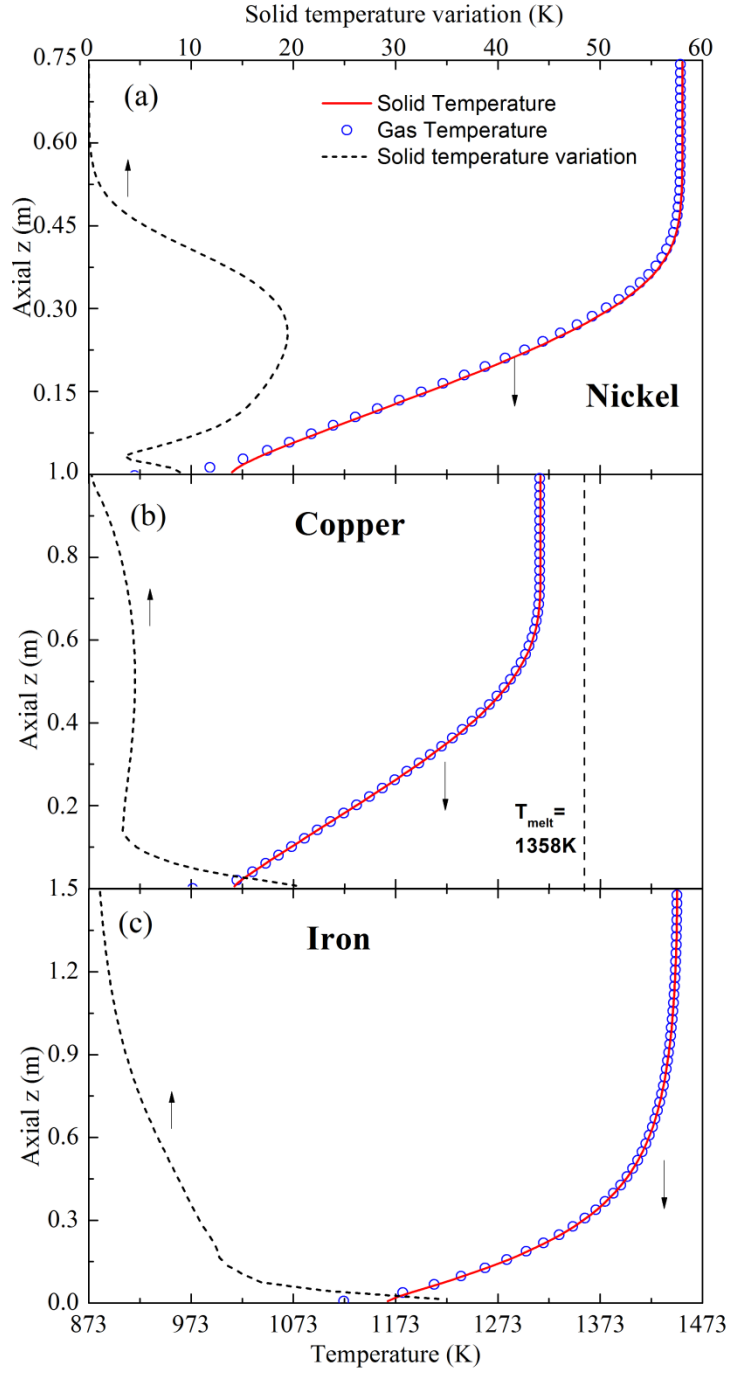


Figure 11 Time-averaged temperature profiles versus the axial position for the solid (lines) and the flow (circles) for (a) nickel-, (b) copper-, and (c) iron-based designs. The dashed lines are the maximum temperature variation of the solid phase in one cycle. In panel b, the melting temperature for copper is also included.

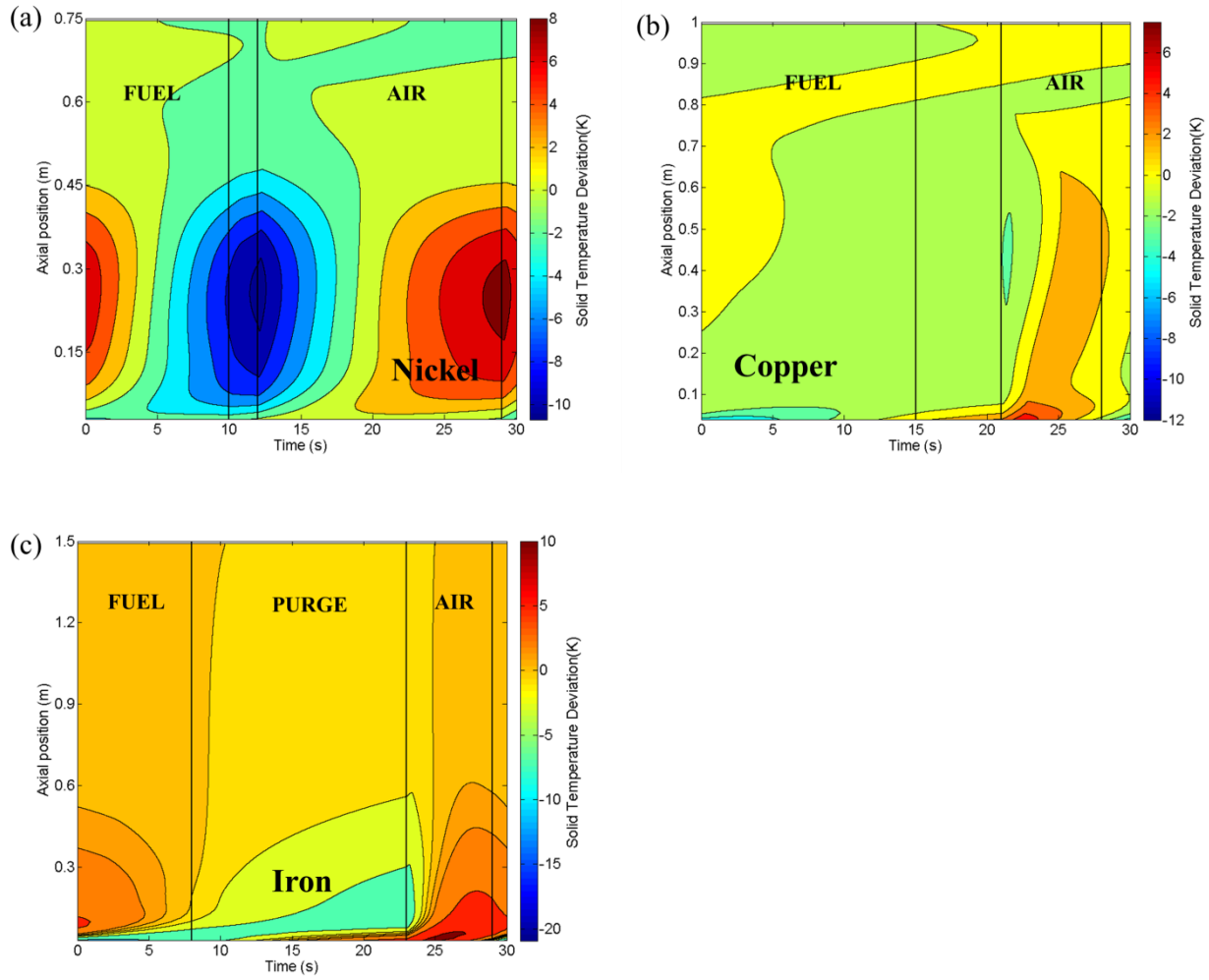


Figure 12 Solid temperature deviation versus time within one cycle for (a) nickel-, (b) copper-, and (c) iron-based designs.



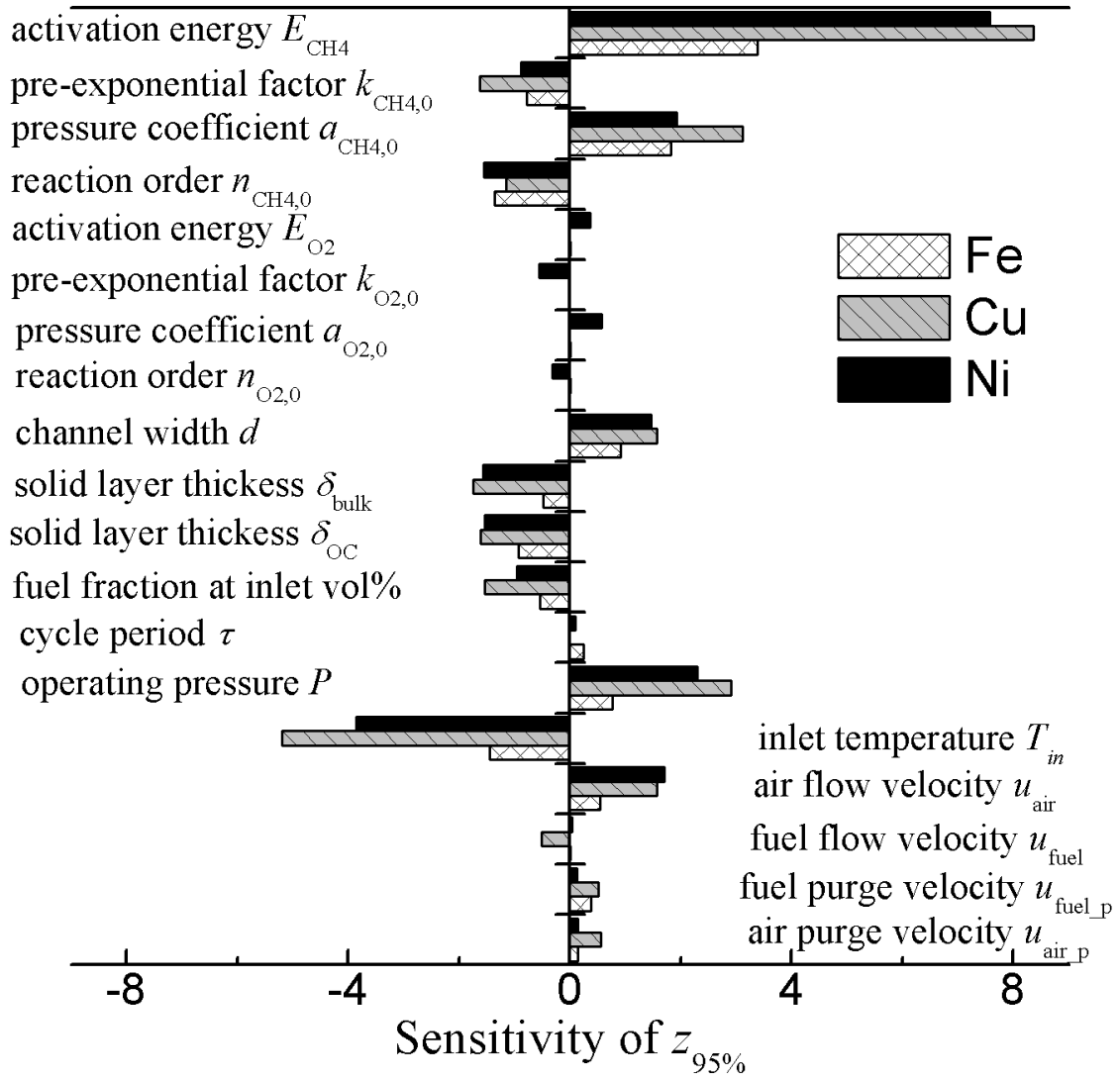


Figure 13 Sensitivity of  $z_{95\%}$  on the reaction kinetics, design parameters and the operating conditions for the three OCs.

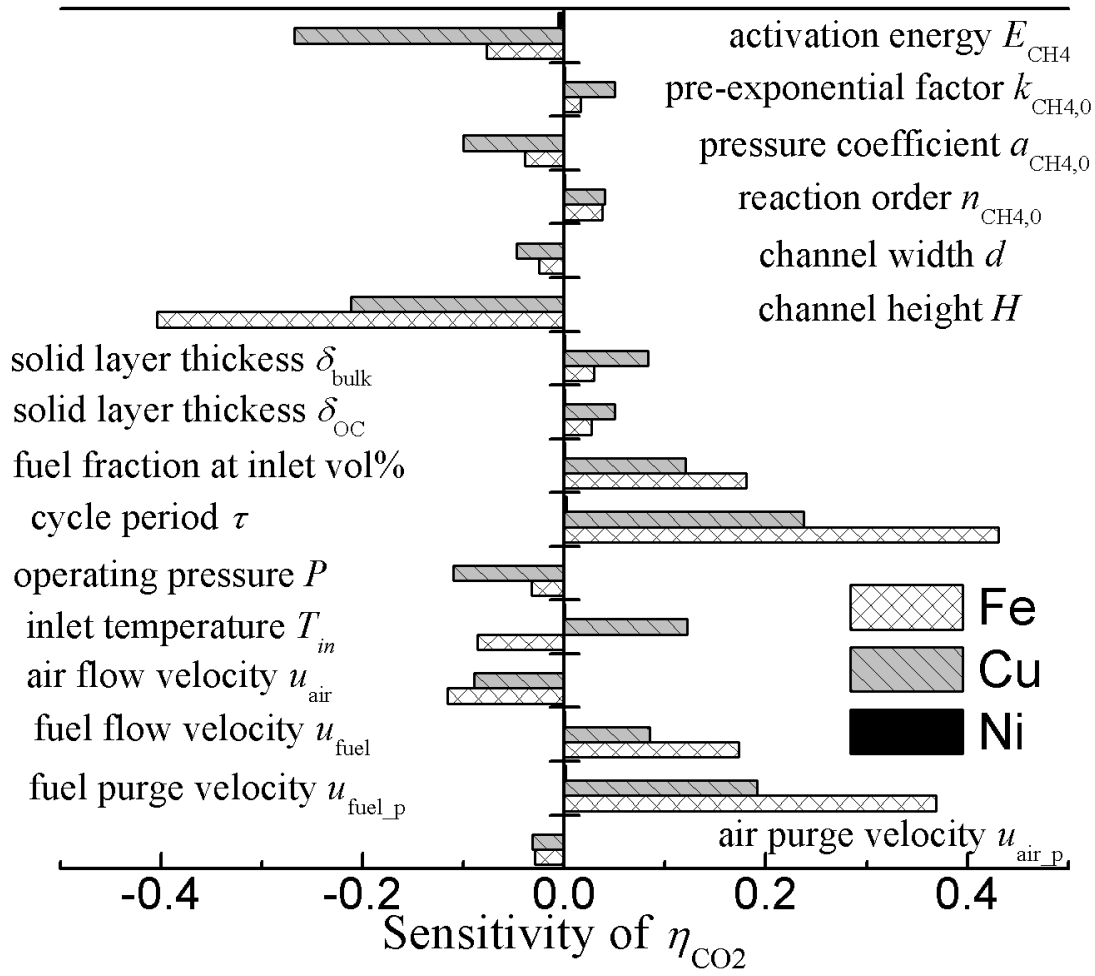


Figure 14 Sensitivity of  $\eta_{\text{CO}_2}$  on the reaction kinetics, design parameters and the operating conditions for the three OCs.

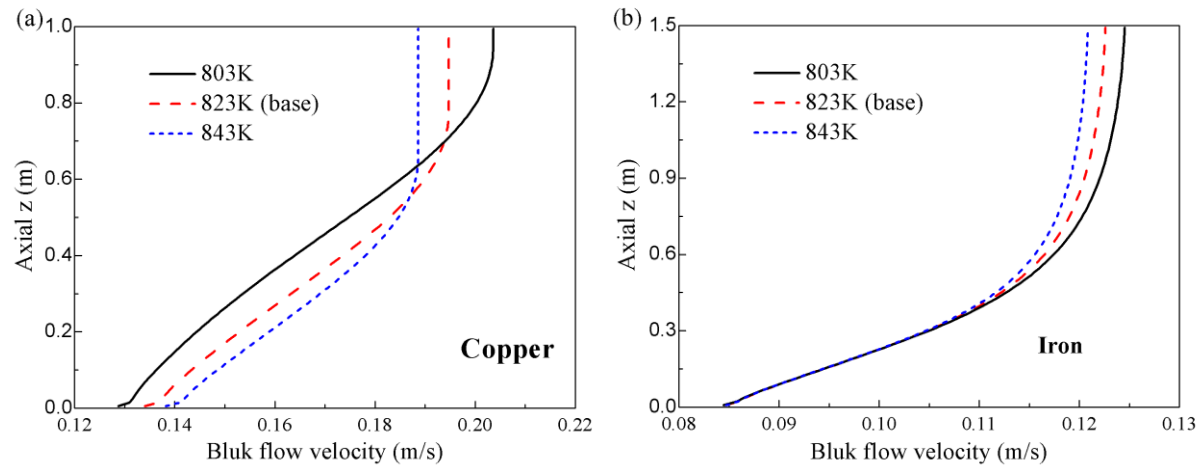


Figure 15 Time-averaged bulk flow velocity within the fuel purge sector for (a) copper and (b) iron at different inlet temperatures.

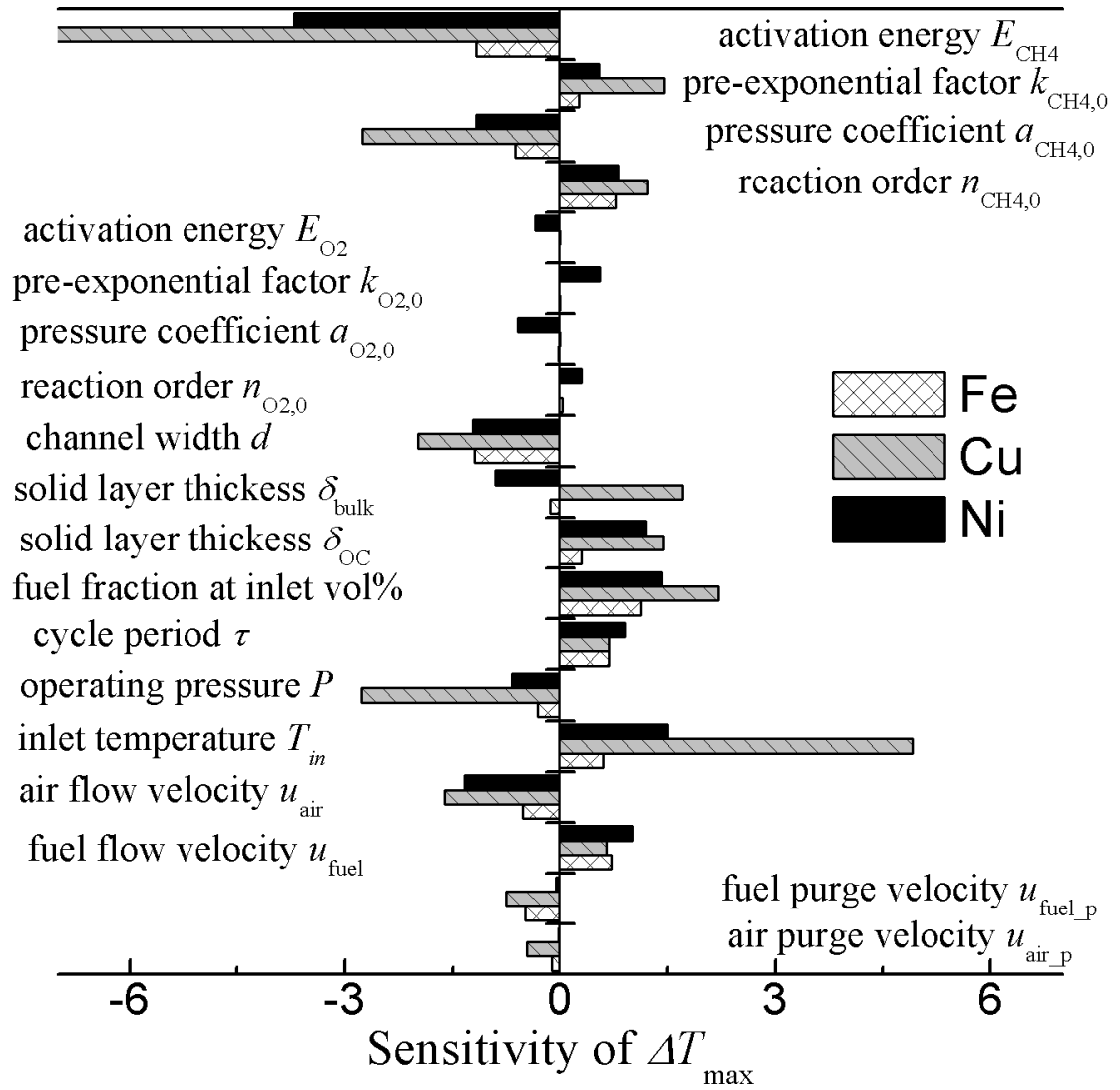


Figure 16 Sensitivity of  $\Delta T_{\max}$  on the reaction kinetics, design parameters and the operating conditions for the three OCs.

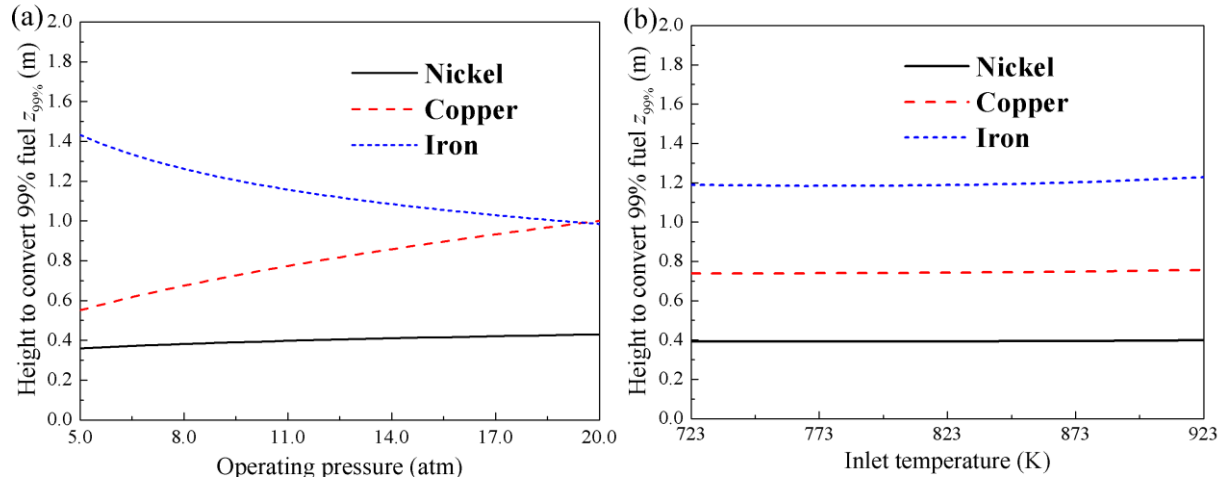


Figure 17  $z_{99\%}$  versus (a) the operating pressure and (b) the inlet temperature for the three OCs.

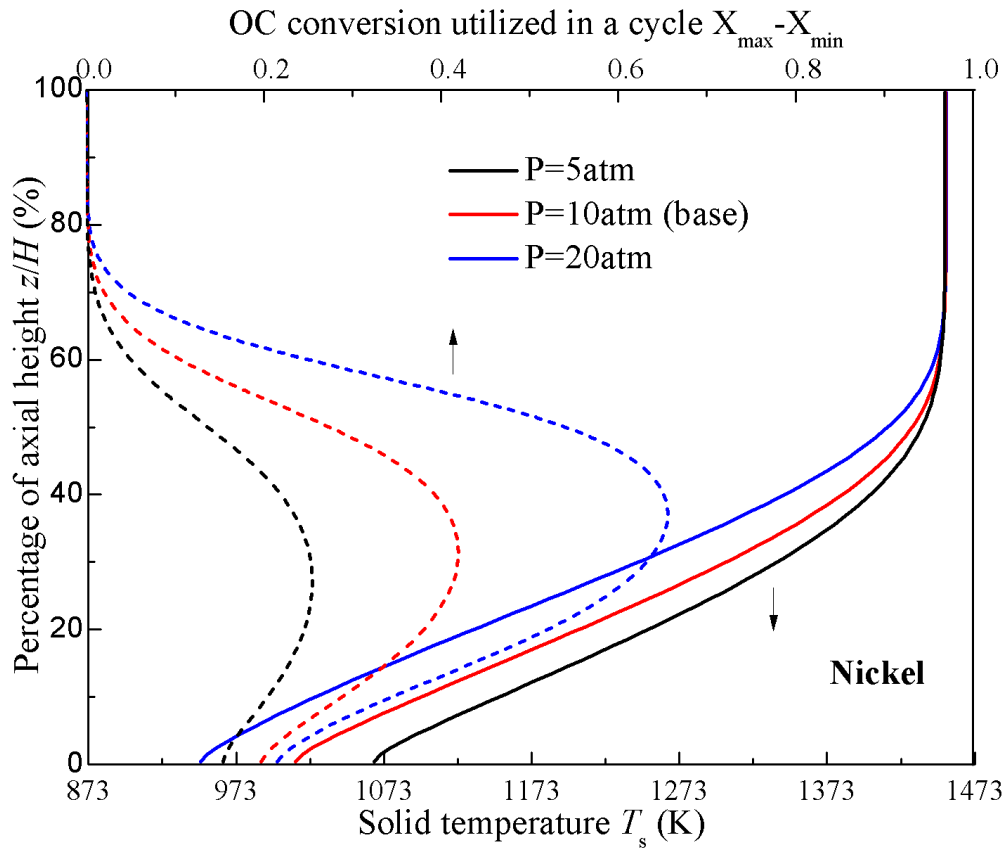


Figure 18 Effects of the operating pressure on the time-averaged solid temperature (solid lines) and the amount oxygen in the OC used (dashed lines) for nickel-based designs within one cycle. Note that the axial position  $z$  is normalized by the height of the design for each operating pressure.

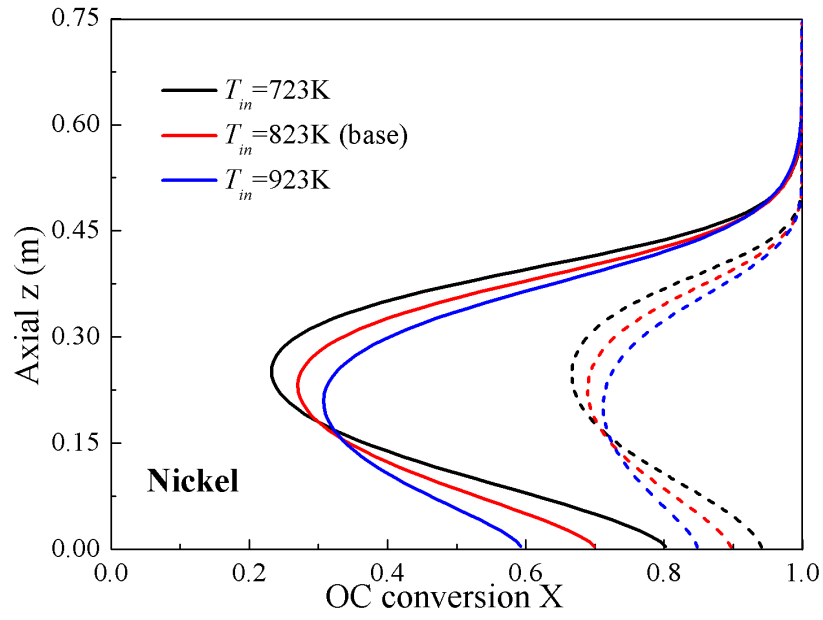


Figure 19 The minimum OC conversion (solid lines) and the maximum OC conversion (dashed lines) for nickel-based designs under different inlet temperatures. The area covered by the maximum and the minimum curves is the same for each case.

Table 1 Properties and kinetics parameters of the OC used in the simulation [15].

OC selected	CuO/Cu	NiO/Ni	Fe <sub>2</sub> O <sub>3</sub> /Fe <sub>3</sub> O <sub>4</sub>
Reduction Oxidation	CH <sub>4</sub> +4CuO→CO <sub>2</sub> +2H <sub>2</sub> O+4Cu O <sub>2</sub> +2Cu→2CuO	CH <sub>4</sub> +4NiO→CO <sub>2</sub> +2H <sub>2</sub> O+4Ni O <sub>2</sub> +2Ni→2NiO	CH <sub>4</sub> +12Fe <sub>2</sub> O <sub>3</sub> →CO <sub>2</sub> +2H <sub>2</sub> O+8Fe <sub>3</sub> O <sub>4</sub> O <sub>2</sub> +4Fe <sub>3</sub> O <sub>4</sub> →6Fe <sub>2</sub> O <sub>3</sub>
melting point <sup>[31]</sup>	1446°C/1085°C	1955°C/1455°C	1565°C/1597°C
Preparation	Wet impregnation	Freeze granulation	Freeze granulation
Active load, $x_{MeO}$	10 wt%	40 wt%	45 wt%
$R_{oc}$	0.02	0.084	0.013
Apparent density, kg m <sup>-3</sup>	1800	3446	3257
Porosity, $\varepsilon_g$	0.57	0.36	0.30
BET surface area, m <sup>2</sup> g <sup>-1</sup>	41.3	0.8	2.5
Particle size, $\mu m$	170	200	150
Reaction rate constant, $k_0, m^{(3n-3)} mol^{(1-n)} s^{-1}$	CH <sub>4</sub> : 1.13×10 <sup>6</sup> O <sub>2</sub> : 2.04×10 <sup>4</sup>	CH <sub>4</sub> : 3.09×10 <sup>6</sup> O <sub>2</sub> : 9.31×10 <sup>3</sup>	CH <sub>4</sub> : 9.23×10 <sup>3</sup> O <sub>2</sub> : 3.58×10 <sup>3</sup>
Reaction order, $n$	CH <sub>4</sub> : 0.4; O <sub>2</sub> : 1.0	CH <sub>4</sub> : 0.8; O <sub>2</sub> : 0.2	CH <sub>4</sub> : 1.3; O <sub>2</sub> : 1.0
Pressure coefficient*, $a$	CH <sub>4</sub> : 0.83; O <sub>2</sub> : 0.68	CH <sub>4</sub> : 0.93; O <sub>2</sub> : 0.46	CH <sub>4</sub> : 1.03; O <sub>2</sub> : 0.84
Activation energy, $E, kJ mol^{-1}$	CH <sub>4</sub> : 60; O <sub>2</sub> : 15	CH <sub>4</sub> : 78; O <sub>2</sub> : 7.0	CH <sub>4</sub> : 49; O <sub>2</sub> : 14

\* Note: the pressure coefficient in ref. [15] is only for reduction with CO or H<sub>2</sub>. There is no available data for CH<sub>4</sub>. A larger coefficient is used for conservative predictions.



Table 2 Base-case designs and operational conditions for the three OCs.

	OC selected	CuO/Cu	NiO/Ni	Fe <sub>2</sub> O <sub>3</sub> /Fe <sub>3</sub> O <sub>4</sub>
	Thermal capacity	1 MW <sub>th</sub>		
Reactor Design	Reactor diameter, $D$	1.70 m	0.97 m	1.50 m
	Reactor height, $H$	1.00 m	0.75 m	1.50 m
	Channel width, $d$	2.00 mm		
	Thickness of OC, $\delta_{oc}$	50 $\mu$ m		
	Thickness of support layer, $\delta_{bulk}$	210 $\mu$ m		
	Fuel sector size, $\theta_{fuel}$ (channel residence time, $\tau_{fuel}$ )	$\pi$ (15s)	$2\pi/3$ (10s)	$8\pi/15$ (8s)
	Fuel purge sector size, $\theta_{fuel\_p}$ (channel residence time, $\tau_{fuel\_p}$ )	$2\pi/5$ (6s)	$2\pi/15$ (2s)	$\pi$ (15s)
	Air sector size, $\theta_{air}$ (channel residence time, $\tau_{air}$ )	$7\pi/15$ (7s)	$17\pi/15$ (17s)	$2\pi/5$ (6s)
	Air purge sector size, $\theta_{air\_p}$ (channel residence time, $\tau_{air\_p}$ )	$2\pi/15$ (2s)	$\pi/15$ (1s)	$\pi/15$ (1s)
Operating Condition	Inlet temperature, $T_{in}$	823 K		
	Operating pressure, $P$	10 atm		
	Inlet fuel volume fraction	15 vol%	25 vol%	50 vol%
	Cycle Period, $\tau$	30 s		
	Flue stream temperature	1314.5 K	1453.3 K	1448.3 K
	Fuel sector feed velocity, $u_{fuel}$ (gas residence time, $t_{fuel}$ )	0.09m/s (6.48s)	0.25m/s (1.44s)	0.065m/s (8.57s)
	Fuel purge feed velocity, $u_{fuel\_p}$ (gas residence time, $t_{fuel\_p}$ )	0.11m/s (5.78s)	0.30m/s (1.46s)	0.06m/s (13.33s)
	Air sector feed velocity, $u_{air}$ (gas residence time, $t_{air}$ )	0.70m/s (1.01s)	1.00m/s (0.49s)	1.00m/s (0.96s)
	Air purge feed velocity, $u_{air\_p}$ (gas residence time, $t_{air\_p}$ )	0.70m/s (0.96s)	1.00m/s (0.47s)	1.20m/s (0.74s)

Note: the inlet velocities are evaluated at the local temperature.

Table 3 Periodic performances and the flue streams from the fuel and air zones for the three OCs.

	OC selected	CuO/Cu	NiO/Ni	Fe <sub>2</sub> O <sub>3</sub> /Fe <sub>3</sub> O <sub>4</sub>
Results	Fuel conversion, $\eta_I$	100.00%	100.00%	99.12%
	location of 99% conversion, $z_{99\%}$	0.70 m	0.49m	1.44 m
	Carbon separation, $\eta_{CO_2}$	98.06%	100.00%	96.89%
	Max. temperature variation, $\Delta T_{\max}$ (axial position with $\Delta T_{\max}$ )	20.3 K (0.0 m)	19.4 K (0.26 m)	34.2 K (0.0 m)
	Fuel feed rate, $\dot{n}_{CH_4}$	1.25 mol/s	1.25 mol/s	1.25 mol/s
	CO <sub>2</sub> feed rate, $\dot{n}_{CO_2}$	7.1 mol/s	3.8 mol/s	1.25 mol/s
	Air feed rate, $\dot{n}_{air}$	30.2 mol/s	34.1 mol/s	28.8 mol/s
	Purge (steam) feed rate, $\dot{n}_{H_2O}$	12.7 mol/s	3.2 mol/s	10.1 mol/s
Fuel Zone	Fuel flue stream velocity, $u_b$	0.10 m/s	0.35 m/s	0.08 m/s
	CH <sub>4</sub> molar fraction, $x_{CH_4}$	0.00%	0.00%	0.11%
	CO <sub>2</sub> molar fraction, $x_{CO_2}$	54.8%	57.47%	25.89%
	H <sub>2</sub> O molar fraction, $x_{H_2O}$	45.2%	42.53%	74.00%
	O <sub>2</sub> molar fraction, $x_{O_2}$	0.00%	0.00%	0.00%
	N <sub>2</sub> molar fraction, $x_{N_2}$	0.00%	0.00%	0.00%
Air Zone	Fuel flue stream velocity, $u_b$	0.58 m/s	0.90 m/s	0.92 m/s
	CH <sub>4</sub> molar fraction, $x_{CH_4}$	0.00%	0.00%	0.00%
	CO <sub>2</sub> molar fraction, $x_{CO_2}$	0.44%	0.00%	0.24%
	H <sub>2</sub> O molar fraction, $x_{H_2O}$	23.28%	5.97%	17.68%
	O <sub>2</sub> molar fraction, $x_{O_2}$	10.59%	13.85%	11.14%
	N <sub>2</sub> molar fraction, $x_{N_2}$	65.69%	80.18%	70.94%

Table 4 Designs and periodic performances for the three OCs under different operating pressure.

The inlet temperature is 823K.

	OC selected	CuO/Cu		NiO/Ni		Fe <sub>2</sub> O <sub>3</sub> /Fe <sub>3</sub> O <sub>4</sub>	
		5 atm	20 atm	5 atm	20 atm	5 atm	20 atm
Design	Reactor height, $H$	0.65 m	1.40 m	0.62 m	0.96 m	1.70 m	1.35 m
	Fuel sector size, $\theta_{fuel}$	$\pi$	$14\pi/15$	$2\pi/3$	$2\pi/3$	$\pi/2$	$2\pi/5$
	Fuel purge sector size, $\theta_{fuel\_p}$	$2\pi/5$	$2\pi/3$	$2\pi/15$	$2\pi/15$	$4\pi/5$	$6\pi/5$
	Air sector size, $\theta_{air}$	$7\pi/15$	$4\pi/15$	$17\pi/15$	$17\pi/15$	$13\pi/20$	$\pi/3$
	Air purge sector size, $\theta_{air\_p}$	$2\pi/15$	$2\pi/15$	$\pi/15$	$\pi/15$	$\pi/20$	$\pi/15$
Operating Condition	Inlet fuel volume fraction	15 vol%		25 vol%		50 vol%	
	Cycle Period, $\tau$	15 s	60s	15s	60s	20s	45s
	Fuel sector feed velocity, $u_{fuel}$	0.18m/s	0.045m/s	0.50m/s	0.13m/s	0.125m/s	0.043m/s
	Fuel purge feed velocity, $u_{fuel\_p}$	0.22m/s	0.045m/s	0.60m/s	0.15m/s	0.123m/s	0.03m/s
	Air sector feed velocity, $u_{air}$	1.40m/s	0.45m/s	2.00m/s	0.50m/s	1.15m/s	0.52m/s
	Air purge feed velocity, $u_{air\_p}$	1.40m/s	0.45m/s	2.00m/s	0.50m/s	2.70m/s	0.75m/s
Results	Fuel conversion, $\eta_I$	100.00%	100.00%	100.00%	100.00%	99.03%	99.05%
	location of 99% conversion, $z_{99\%}$	0.46 m	1.01m	0.40m	0.65m	1.68 m	1.32m
	Flue stream temperature	1313.3 K	1315.2 K	1452.9K	1453.7K	1444.6 K	1449.6K
	Carbon separation, $\eta_{CO2}$	100.00%	95.16%	100.00%	99.04%	95.88%	96.10%
	Max. temperature variation, $\Delta T_{max}$	18.0 K	24.3K	11.9 K	30.1K	18.8 K	44.0K

Table 5 Designs and periodic performances for the three OCs under different inlet temperature.

The operating pressure is 10 atm.

	OC selected	CuO/Cu		NiO/Ni		Fe <sub>2</sub> O <sub>3</sub> /Fe <sub>3</sub> O <sub>4</sub>	
		723 K	923 K	723 K	923 K	723 K	923 K
Design	Reactor height, $H$	1.00m	1.00m	0.75m	0.75m	1.50m	1.50m
	Fuel sector size, $\theta_{fuel}$	$14\pi/15$	$\pi$	$2\pi/3$	$2\pi/3$	$8\pi/15$	$8\pi/15$
	Fuel purge sector size, $\theta_{fuel\_p}$	$\pi/2$	$2\pi/5$	$2\pi/15$	$2\pi/15$	$\pi$	$\pi$
	Air sector size, $\theta_{air}$	$7\pi/15$	$7\pi/15$	$17\pi/15$	$17\pi/15$	$2\pi/5$	$2\pi/5$
	Air purge sector size, $\theta_{air\_p}$	$\pi/10$	$2\pi/15$	$\pi/15$	$\pi/15$	$\pi/15$	$\pi/15$
Operating Condition	Inlet fuel volume fraction	19vol%	12.5vol%	29vol%	21vol%	58vol%	42vol%
	Cycle period	30s					
	Fuel sector feed velocity, $u_{fuel}$	0.066m/s	0.12m/s	0.19m/s	0.33m/s	0.05m/s	0.085m/s
	Fuel purge feed velocity, $u_{fuel\_p}$	0.077m/s	0.14m/s	0.23m/s	0.40m/s	0.05m/s	0.064m/s
	Air sector feed velocity, $u_{air}$	0.54m/s	1.00m/s	0.76m/s	1.33m/s	0.75m/s	1.33m/s
	Air purge feed velocity, $u_{air\_p}$	0.54m/s	1.00m/s	0.76m/s	1.33m/s	1.00m/s	1.5m/s
Results	Fuel conversion, $\eta_I$	100.00%	100.00%	100.00%	100.00%	99.22%	99.00%
	location of 99% conversion, $z_{99\%}$	0.71m	0.70m	0.49m	0.50m	1.38m	1.49m
	Flue stream temperature	1314.3K	1314.8K	1457.7K	1450.5K	1443.2K	1455.3K
	Carbon separation, $\eta_{CO2}$	97.24%	99.85%	99.82%	100.00%	95.80%	95.45%
	Max. temperature variation, $\Delta T_{max}$	24.2K	17.0K	20.6K	18.2K	37.7K	30.5K

## Appendix A

For an isothermal, steady-state reactive flow, the species equation (5) can be simplified to:

$$A_p C_{tot} \frac{d(ux_i)}{dz} = P_c \omega_i, \quad i = \text{CH}_4, \text{CO}_2, \text{ or } \text{H}_2\text{O} \quad (\text{A1})$$

where  $C_{tot}$  is overall concentration of the bulk flow calculated by ideal gas law. The overall mass conservation equation for the bulk flow can be obtained by summing Eq. (A1):

$$A_p C_{tot} \frac{du}{dz} = P_c \sum_i \omega_i \quad (\text{A2})$$

The reaction rate is calculated according to Eqs.(1) and (2) with the assumption that the OC remains fully oxidized:

$$\frac{\omega_i}{v_i} = \frac{\delta_{oc} \varepsilon_{oc} \hat{\rho}_{m,i}}{v_{oc}} \frac{dX_{oc}}{dt} = \delta_{oc} \varepsilon_{oc} k_p C_{tot}^n x_{CH_4}^n \quad (\text{A3})$$

where  $k_p = (P/P_0)^{-a} k_0 \exp(-E/R_u T)$ . Substitute (A3) into (A1) and (A2), we can obtain:

$$\frac{d[u(2x_{CH_4} + 1)]}{dz} = 0 \quad (\text{A4})$$

$$\frac{y^n dy}{(1-y)^n dz} = \frac{P_c \delta_{oc} \varepsilon_{oc} k_p C_{tot}^{n-1}}{2^{n-1} A_p u_0 (2x_{CH_4,0} + 1)} \quad (\text{A5})$$

where  $y = (2x_{CH_4} + 1)^{-1}$ . Thus, integrate (A5), we can obtain the fuel concentration profile as expressed by Eq. (4)